Geochemistry, Geophysics, Geosystems®

RESEARCH ARTICLE
10.1029/2024GC011651

A REE Inverse Model From Bulk Distribution Coefficients and Boundary Conditions: Results for Shield and Rejuvenated Stage Hawaiian Volcanoes

M. J. Carr[1], **M. D. Feigenson**[1], and **E. Gazel**[2]

[1]Department of Earth and Planetary Sciences, Rutgers University, Piscataway, NJ, USA, [2]Department of Earth and Atmospheric Sciences, Cornell University, Ithaca, NY, USA

Abstract A major challenge in mantle geochemistry is determining the source composition and melt fraction involved in melting. We provide a new Rare-Earth Element (REE) inverse model that provides source concentration, source and melt mineral modes, and melt fraction based on the difference between separate determinations of bulk distribution coefficients and constrained by boundary conditions. An analytical inverse of the batch melting equation provides expressions for source, C_o^i, and bulk distribution coefficient of the mantle, D_o^i, with two unknowns, the initial concentration of La in the mantle, C_o^{La}, and P^i, the bulk distribution coefficient of the melt. We traverse through a range of C_o^{La} steps and examine thousands of melt modes, P^i, at each step. Thousands of trial melt modes fail by generating D_o^i that are inconsistent with partition coefficients. Many surviving trials cannot be inverted to estimate a mantle mode. Other boundary conditions eliminate even more trials. Surviving trials are ordered by the difference between D_o^i calculated from the REE data of a lava suite and D_c^i calculated from partition coefficients and mantle mode. We select the solution with the closest fit that passes all the boundary conditions. We tested our new model with lava suites from Hawaii where different lines of evidence suggest that they melted from different mantle sources, Mauna Kea representing shield-stage lava and submarine Kiekie representing rejuvenated stage lava. Our inverse determination of mantle composition and melting parameters was consistent with earlier models based on assumptions of HREE composition.

Plain Language Summary Determining the composition of our planet's interior is a major goal of geochemistry. The most common approach is to make forward models based on reasonable assumptions about the source composition and the melting process to calculate synthetic compositions that match the observed lava. Successful forward models may be difficult to achieve, but nevertheless remain dependent on initial assumptions. In principle, inverse models make fewer assumptions and achieve more objective results. Even so, most published inverse models for mantle melting require assumptions about the source. The inverse modeling described here relies on boundary conditions and the match between observed and calculated bulk distribution coefficients to determine the behavior of mantle parameters as a function of the initial lanthanum concentration (C_o^{La}). Certain behavior patterns allow determination of the optimum C_o^{La}, allowing a complete inverse. Successful inverse models for Hawaiian lava suites define two distinct mantle types, in agreement with past observations about these volcanoes.

Key Points:

- Melt modes and mantle La concentrations generate trial source and bulk distribution profiles, but most solutions fail boundary conditions
- Trial solutions are ranked by comparing observed and calculated bulk distribution profiles. The best fit over a range of La is the solution
- Optimum source and bulk distribution profiles provide melt extents for shield stage Hawaiian tholeiites and rejuvenated basalts

Supporting Information:

Supporting Information may be found in the online version of this article.

Correspondence to:

M. J. Carr,
carrvolcano@gmail.com

Citation:

Carr, M. J., Feigenson, M. D., & Gazel, E. (2024). A REE inverse model from bulk distribution coefficients and boundary conditions: Results for shield and rejuvenated stage Hawaiian volcanoes. *Geochemistry, Geophysics, Geosystems*, *25*, e2024GC011651. https://doi.org/10.1029/2024GC011651

Received 16 MAY 2024
Accepted 24 JUL 2024

1. Introduction

Elucidating the source composition that melts to produce a suite of samples collected on the planet's surface is one of the major challenges in mantle geochemistry. While forward modeling from an assumed source composition allows fast hypothesis testing, the source mineralogy and melt fractions will always be significant unknowns. Thus, results will always depend on the assumptions used. Inverse modeling promises a more robust alternative, especially models taking advantage of the smoothly related properties of the Rare-Earth Elements (REE). Minster and Allègre (1978) proposed a method for inverting the REE concentrations in a related suite of lavas based on the batch melting equation. Using insights from process identification diagrams (Treuil & Joron, 1975), they obtained an analytical solution by assuming that a highly incompatible or hygromagmatophile element has an effective partition coefficient of zero. Assuming batch melting and perfect incompatibility of La allows simple expressions for the source concentration (C_o^i) and the bulk distribution coefficient $\left(D_o^i\right)$ based on the slopes (S^i) and intercepts (I^i) of process identification diagrams, the bulk distribution coefficient for minerals entering the melt (P^i) and relative degrees of partial melting. The slopes, intercepts, and degrees of melting (F) were obtained by using all the data simultaneously with optimization by least squares fit.

Clague and Frey (1982) applied the Minster and Allègre (1978) logic to carefully chosen pairs of elements with Th as the hygromagmatophile element. To obtain C_o^i and D_o^i values for the REE, they assumed realistic values of P^i and further assumed that the HREE (e.g., Lu) in the mantle had a concentration of 2–4 times chondritic. This allowed the estimation of F, the extent of melting, and subsequent calculation of source values and bulk distribution coefficients. Later, Albarède (1983), Albarède and Tamagnan (1988), and Frey et al. (1991) provided a simplified inversion based on the batch melting equation. This model solves for source compositions and proportions of residual clinopyroxene and garnet. Because the number of samples is typically larger than the number of elements and the number of phases, the problem is overdetermined. Solutions can be obtained using least squares provided that the minerals with low affinity for the REE (olivine, spinel, and orthopyroxene) are subject to external constraints from petrology or geophysics. This work highlighted the problem posed by minerals with low affinity for the REEs, especially olivine, a major mantle constituent.

It is important to keep in mind that while batch melting allows simple equations for C_o^i and D_o^i it may be less physically realistic than other melting models. Langmuir et al. (1977) showed that batch melting does not explain the REE profiles of MORB and proposed continuous melting. McKenzie and O'Nions (1991) developed a physics based fractional melting scenario. The physics of melt generation and separation from the mantle matrix indicates that melts separate at very low degrees of melting. In this fractional melting scenario, melt fraction and melt separation vary as a function of depth. Observed variations in lava produced in large magmatic systems are much smaller than the variations in individual primary fractional melts; therefore, there must be a large-scale aggregation of small melt portions. McKenzie and O'Nions (1991) used average melt compositions as input. They estimated source compositions and mineralogy based on the bulk composition of the silicate part of the earth and solved for the melt extraction profile as a function of depth using aggregated fractional melting (Albarède, 1995; Shaw, 1970).

Melt generation processes can also be studied through inverse models based on trace element contents of clinopyroxenes in residues or peridotites (e.g., Liu & Liang, 2017; Zou, 1997). These methods are particularly useful for mid-ocean ridge basalts (MORB). To explain the REE patterns in residual clinopyroxenes, Zou (1997) and Liu and Liang (2017) call for disequilibrium melting. These inverse models are entirely different from the batch melting thread because residues are the focus rather than melts, and disequilibrium is assumed rather than equilibrium melting. Recently, Liu and Liang (2017) and Brown et al. (2020) introduced Markov chain Monte Carlo (MCMC) methods to inverse problems related to mantle melting. Oliveira et al. (2021) go further by incorporating an adaptive MCMC algorithm in a complex inverse that includes a model of two-phase multicomponent reactive transport, the thermodynamic evolution of major elements and mineral phases and a disequilibrium model of trace element partitioning.

The batch melting approach initiated by Minster and Allègre (1978) and pursued by others is not widely used. Our earliest attempt (Hofmann & Feigenson, 1983) used the analytical approach of Minster and Allègre (1978) but did not seek a simultaneous least squares solution. Instead, calculations were made on an element-by-element basis, following the simpler approach of Clague and Frey (1982). The Hofmann and Feigenson (1983) method made no assumptions about the absolute concentrations of the HREE and made clear that the assumption of perfect incompatibility that allows the analytical solution to the batch melting equation gives rise to a scalar, the initial concentration of the element assumed to be perfectly incompatible. This scalar modifies both the source vector and the bulk distribution vector and prevents their absolute determination. In subsequent publications, Feigenson et al. (1996) employed a full suite of REEs and adopted La as the perfectly incompatible element. Feigenson et al. (2003) applied a Monte Carlo approach to select melt modes and then rejected modes that generated unrealistic D_o^{HREE} estimates, leaving a narrow field of acceptable D_o^i vectors. Although boundary conditions refined the shapes of the C_o^i and D_o^i profiles, there was no progress on determining the value of the scalar quantity, the initial concentration of La in the mantle, C_o^{La}, and so the positions of the C_o^i and D_o^i profiles within a REE diagram were not constrained.

The batch melting inverse equations of Minster and Allègre (1978) produce C_o^i and D_o^i profiles from input P^i profiles but without guidance on which input profile to select or what value of C_o^{La} to use. Assuming a P^i and C_o^{La} would be a forward model. Similarly, assumptions about the likely compositions of the HREE in a source are an unsatisfactory way forward. Instead, we realized that the D_o^i profile from the inverse equations allows estimation of a mantle mode. Multiplying the estimated mode by appropriate partition coefficients provides a calculated bulk distribution coefficient, D_c^i. If the input P^i profile and the choice of C_o^{La} are correct, then (D_o^i–D_c^i) will be minimized. Our initial attempt, based on minimizing (D_o^i–D_c^i), varied C_o^{La} by stepping through a range. At each step we looked at 1,300 melt modes and minimized (D_o^i–D_c^i) using least squares to solve for four melt mode and four mantle mode minerals assuming a lherzolite mantle. For synthetic melt suites made without error this approach successfully returned the input with high precision but the fits were unrealistically close, around 10^{-12}. Adding an error caused complete collapse. Attempts to find the cause of the failure led to a constrained solution with nine boundary conditions. The model has two parts; boundary conditions that remove most potential solutions; followed by minimization of (D_o^i–D_c^i) to select the best fit among the remaining potential solutions. Because of the centrality of the bulk partition coefficients of mantle ($\boldsymbol{D}$) and melt ($\boldsymbol{P}$), these vectors, $\boldsymbol{D}_o^i$, $\boldsymbol{D}_c^i$, $\boldsymbol{P}^i$, are in bold from here forward. Note that $\boldsymbol{D}_c^i$ and $\boldsymbol{P}^i$ are standard calculations; mineral modes times partition coefficients. $\boldsymbol{D}_o^i$ is calculated from the slopes and intercepts of process identification diagrams (Minster & Allègre, 1978).

To test our new model, we examined suites of Hawaiian lava thought to be melted from different mantle sources. We revisit our analysis of the Mauna Kea (MK) high silica suite in the Hawaiian Scientific Drilling Program (HSDP2). This exceptional sample and data set is ideal for attempting an inverse model (DePaolo et al., 1999; DePaolo & Stolper, 1996). We also briefly examine 17 samples from Mauna Loa (ML) from the upper section of the drill core. We looked at several suites of post-erosional, rejuvenated magmas and found the submarine Kiekie (KK) suite (Dixon et al., 2008) suitable for the inverse. Finally, we made several synthetic magma suites to understand the effects of boundary conditions and to check whether the inverse model returns the input, as a validation test. The goal of this study was to produce a quantitative inverse model that provides the source REE concentration, source and melt mineral modes, and melt fraction based on bulk distribution coefficients and constrained by boundary conditions. We review the necessary mathematical formulization and our selection of partition coefficients and explain our correction for the LREE. Because we compare D profiles with very small differences, we use the best possible data and make careful corrections for fractionation.

The software makes a double search. The outer search is a traverse that steps through a range of C_o^{La}. At each step thousands of potential melt modes are tried. Applying boundary conditions eliminates most trials and allows optimization of ($\boldsymbol{D}_o^i$–$\boldsymbol{D}_c^i$) to identify the best model among survivors. Stringing together C_o^{La} steps defines distinctive inverse paths through mantle mode and melt mode space. The behavior of the inverse path allows selection of C_o^{La}. The software that enables this process, Igpet (Carr & Gazel, 2017), is freely available online at https://sites.google.com/site/tsigpetteaching/.

2. Mathematical Formulation

2.1. Process Identification and Inverse Equations

Process identification diagrams (Treuil & Joron, 1975) are the starting point of the inverse. For the x axis, we use La_N as a highly incompatible or hygromagmatophile element. The y variable is La_N/REE_N, where REE are the 13 remaining rare earths and the subscript $_N$ denotes chondrite normalized units. Figure 1a is a typical process identification diagram. The equation of the regression line is:

$$C_l^{La}/C_l^i = S^i C_l^{La} + I^i \qquad (1)$$

C_l^i is concentration in the melt.

The 13 REEs from Ce to Lu define slope and intercept vectors that can be understood in terms of the batch melting equation. The analytical data for 13 REEs in 59 MK samples are converted into four 13 element vectors: slope, slope error, intercept, and intercept error. Figure 1b is a graphical summary of all the well-corrected REE data for the HSDP2 high silica group from Mauna Kea. Figure 1c compares the slope and intercept vectors of three Hawaiian suites, Mauna Kea, submarine Kiekie and Mauna Loa. The process identification statistics for Mauna Kea and submarine Kiekie are in Table S1 in Supporting Information S3. The intercept errors are larger for the HREE, and the slope errors are larger for the LREE. This appears related to the geometry of the process

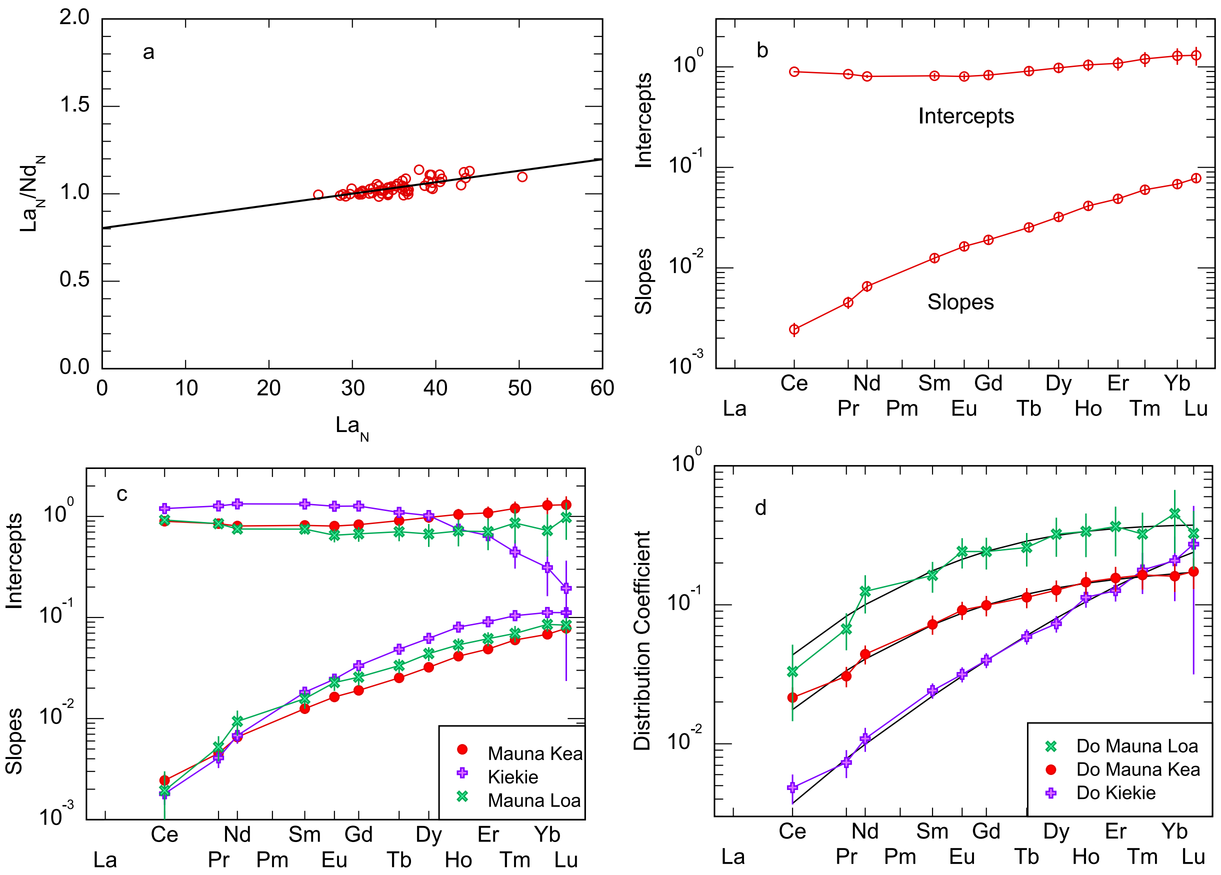

Figure 1. Process identification and D_o^i (a) Process identification diagram for Mauna Kea defines slope and intercept for Nd. REEs normalized ($_N$) to the chondritic values of McDonough and Sun (1995). (b) Slope, S^i, and intercept, I^i, vectors for Mauna Kea. Error bars represent one standard error of intercept and slope.
(c) Comparison of slope and intercept profiles for three Hawaiian suites. Intercepts for LREE are close to 1 and slopes are very shallow but should be positive. The HREE are more variable because the main stage tholeiites have very little garnet and Kiekie has a moderate amount. (d) $\boldsymbol{D}_o^i$ profiles for Mauna Kea (red), Mauna Loa (green) and Kiekie (purple). Calculated profiles, $\boldsymbol{D}_c^i$, are smooth black lines slipping through the observed profiles. Error bars propagated from the S^i and I^i vectors in c. The profiles are for the minimum D_{fit} at C_o^{La} steps near the best solutions. C_o^{La} is 2.0 for Kiekie, 4.85 for Mauna Kea, 10.0 for Mauna Loa.

identification diagrams. Figure 1d uses Equation 8 (described below) to calculate bulk distribution coefficients for the mantle (Table S2 in Supporting Information S3). The error bars in Figure 1d are propagated from the slope and intercept errors and an estimated 9% error in C_o^{La}.

Define terms:

Abbreviations for the four major lherzolite minerals are; gt, cpx, ol, opx

Parameters are grouped by input (first), assumptions (second), results to test (third)

The primary input data, C_l^i, determine the fixed vectors S^i and I^i using Equation 1.

C_l^i	REE concentrations in melt l, $i = 14$, including La (primary input data)
S^i	slopes from process identification regressions, $i = 13$
I^i	intercepts from process identification regressions, $i = 13$

Assumptions (partition coefficient matrix, a grid of melt modes and a range of C_o^{La} values) define trial C_o^i and $\boldsymbol{D}_o^i$ profiles that are then subjected to numerous tests.

M_j^i	partition coefficient matrix for 14 REE in 4 minerals (Table 1)
p^j	a trial melt mode; Pgt, Pcpx, Pol, Popx

Table 1
Partition Coefficients and Initial Slope, Intercept Adjustments

						Initial adjustments	
	Ionic radius	Garnet	Clino-pyroxene	Ortho-pyroxene	Olivine	Slope	Intercept
La	1.172	0.003	0.046	1.00E-03	1.20E-05		
Ce	1.150	0.012	0.108	2.60E-03	4.19E-05	1.645	0.967
Pr	1.130	0.041	0.204	5.70E-03	1.21E-04	1.221	0.967
Nd	1.123	0.061	0.246	7.30E-03	1.74E-04	1.164	0.967
Sm	1.098	0.222	0.423	1.67E-02	5.81E-04	1.063	0.967
Eu	1.087	0.367	0.504	2.31E-02	9.57E-04	1.043	0.967
Gd	1.078	0.537	0.566	2.96E-02	1.42E-03	1.032	0.967
Tb	1.063	0.956	0.648	4.33E-02	2.66E-03	1.020	0.967
Dy	1.052	1.394	0.686	5.59E-02	4.13E-03	1.014	0.967
Ho	1.041	1.960	0.700	7.05E-02	6.29E-03	1.010	0.967
Er	1.030	2.656	0.690	8.71E-02	9.41E-03	1.007	0.967
Tm	1.020	3.394	0.661	1.04E-01	1.34E-02	1.005	0.967
Yb	1.008	4.385	0.606	1.25E-01	2.00E-02	1.003	0.967
Lu	1.001	4.995	0.565	1.38E-01	2.50E-02	1.002	0.967

Note. Experimental data adjusted to parabolic shape based on ionic radius. Sources: garnet- Van Westeren et al. (1999); clinopyroxene- Hauri et al. (1994); orthopyroxene- Kelemen et al. (1992); olivine- Beattie (1994).

$\boldsymbol{P}^i$ bulk distribution coefficients for minerals entering the melt calculated from $p^jM_j^i$

C_o^{La} initial La concentration in the mantle, a scalar

Trial values to test and sort primarily involve $\boldsymbol{D}_o^i$, d^j and D_{fit}

C_o^i initial REE concentrations in the mantle, the source vector

$\boldsymbol{D}_o^i$ bulk distribution coefficients for the mantle calculated from S^i and I^i

d^j estimated mantle mode: Dgt, Dcpx, Dol, Dopx

$\boldsymbol{D}_c^i$ bulk distribution coefficients for the mantle calculated from $d^jM_j^i$

D_{fit} error estimate based on $D_o^i – D_c^i$ (Equation 13)

Dol# 100 × olivine/(olivine + orthopyroxene) for the mantle mode

Pol# 100 × olivine/(olivine + orthopyroxene) for the melt mode

Xol# maximum Dol# allowed, default is 100

F^i melt proportions calculated from REE

F average melt proportion based on Ce through Ho

The equation for batch melting is:

$$C_l^i = C_o^i / \left(\boldsymbol{D}_o^i + F\left(1 - \boldsymbol{P}^i\right)\right) \tag{2}$$

For the highly incompatible element La, assume $\boldsymbol{D}_o^i$ and $\boldsymbol{P}^i$ are zero so:

$$C_l^{La} = C_o^{La} / F \tag{3}$$

Divide 3 by 2, then rearrange and substitute in 3 to remove F and obtain:

$$C_l^{La}/C_l^i = \left(\boldsymbol{D}_o^i/C_o^i\right) C_l^{La} + C_o^{La}\left(1 - \boldsymbol{P}^i\right)/C_o^i \tag{4}$$

Define the slope and intercept vectors as

$$S^i = \boldsymbol{D}_o^i/C_o^i \tag{5}$$

$$I^i = C_o^{La}\left(1 - \boldsymbol{P}^i\right)/C_o^i \tag{6}$$

and obtain $C_l^{La}/C_l^i = S^i C_l^{La} + I^i$, the equation for the process identification diagrams.

Rearrange 5 and 6 to define the source (C_o^i) and bulk distribution coefficient (D_o^i) relative to C_o^{La}.

$$C_o^i = C_o^{La} * \left(1 - \boldsymbol{P}^i\right)/I^i \tag{7}$$

$$\boldsymbol{D}_o^i = C_o^{La} * S^i\left(1 - \boldsymbol{P}^i\right)/I^i \tag{8}$$

Equations 7 and 8 include the scalar quantity C_o^{La}, the chondrite normalized concentration of La in the mantle. Assuming $C_o^{La} = 1.0$, for chondritic abundance, provides an estimate of the shape of C_o^i and $\boldsymbol{D}_o^i$. The shape of a C_o^i vector allows qualitative interpretations such as a flat, enriched, or depleted source. Similarly, the steepness of a $\boldsymbol{D}_o^i$ profile in the HREEs allows qualitative estimates of the amount of garnet in the source. A reasonable estimate of C_o^{La} would allow quantitative information.

The melt proportion was lost in Equation 4 but can be recovered by solving for F in the batch melt equation. For each REE an estimated F is obtained.

$$F^i = \left(C_o^i/C_l^i - \boldsymbol{D}_o^i\right)/\left(1 - \boldsymbol{P}^i\right) \tag{9}$$

Substitute Equations 7 and 8 into 9 to obtain F^i in terms of C_o^{La}, slope, intercept and C_l^i.

$$F^i = C_o^{La} * \left(1/C_l^i - S^i\right)/I^i \tag{10}$$

Each REE provides an estimate of F, but the HREEs have intercepts that approach zero so, in practice, only the estimates from Ce to Er are useful to determine an average melt proportion.

By determining the value of C_o^{La}, Equations 7, 8, and 10 will provide actual values rather than relative values. Part of our approach to solving for C_o^{La} is the comparison of observed and calculated versions of the bulk distribution coefficient of the mantle. The observed version, Equation 8, includes the invariant vectors, S^i and I^i, derived from analytical data collected on lava suites, a variable constant, C_o^{La}, and a variable vector, $\boldsymbol{P}^i$, the bulk distribution coefficient of the minerals entering the melt. $\boldsymbol{P}^i$ is a variable input selected from a grid of trial melt modes. For any value of C_o^{La} and any trial $\boldsymbol{P}^i$ vector, we obtain a trial or observed $\boldsymbol{D}_o^i$. An estimated mantle mode, d^j, can be determined from the trial $\boldsymbol{D}_o^i$ by solving the two equations in Equation 11 for d^j using least squares.

$$\boldsymbol{D}_o^i = \sum_j d^j M_j^i \text{ and } \sum_j d^j = 1 \tag{11}$$

If the solution includes a negative mantle mineral proportion, the trial fails. If all the mineral proportions are positive then we can calculate $\boldsymbol{D}_c^i$.

$$\boldsymbol{D}_c^i = \sum_j d^j M_j^i \tag{12}$$

If our choice for C_o^{La} and melt modes coincide with what the mantle produced, the observed and calculated bulk distribution coefficients vectors will be the same. Therefore, we compare the two versions of the bulk distribution coefficient for the mantle (Equations 8 and 12) to make a fit test, D_{fit} (Equation 13), for ranking possible solutions.

We divide ($\boldsymbol{D}_o^i$–$\boldsymbol{D}_c^i$) by C_o^{La} to cancel the C_o^{La} term in $\boldsymbol{D}_o^i$, allowing a focus on profile shape rather than profile height.

$$D_{fit} = \sum_{i=1}^{13} \left(\frac{\boldsymbol{D}_o^i - \boldsymbol{D}_c^i}{C_o^{La}} \right)^2 \qquad (13)$$

Equation 11 is a system with four unknown mantle mineral proportions and 13 equations (REE data minus La) solvable by least squares, but there is an additional complication. Olivine and orthopyroxene have sufficiently similar partition coefficients that solving for four mineral proportions can generate large proportions for ol and opx that are similar in scale but opposite in sign. Negative minerals make no sense here, so ol and opx are replaced by the mafic sum, ol + opx and Equation 11 is solved for three minerals. To obtain estimates of ol and opx, we make a blended partition coefficient varying *Dol#* between 0 and a maximum, *Xol#*, normally 100. A golden section optimization finds the minimum D_{fit} in the *Dol#* range using a tolerance of 1%, or 0.5% for improved precision. Iterations are limited to 10.

We compare the slope, S^i, and intercept, I^i, vectors in Figure 1c. Mauna Kea has the smoothest slope and intercept profiles with the shortest error bars. Kiekie has smooth profiles as well but large error bars for the HREE intercepts. Mauna Loa is included to show profiles that are not smooth. Furthermore, Mauna Loa's error bars are larger. Figure 1d applies Equations 8 ($\boldsymbol{D}_o^i$) and 12 ($\boldsymbol{D}_c^i$) to the lowest D_{fit} at the C_o^{La} step identified as optimum for the three suites. The diagram reveals the relative quality of the three suites and cautions against proceeding with weak data. D_{fit} is the difference between the colored $\boldsymbol{D}_o^i$ profiles and the thin black $\boldsymbol{D}_c^i$ profiles. The contrast in D_{fit} between Mauna Kea (9.2×10^{-6}) and Mauna Loa (1.4×10^{-4}) is clear. Mauna Kea has the lowest D_{fit} because its $\boldsymbol{D}_o^i$ is smooth. Kiekie is weaker (8.1×10^{-5}) because of large error bars in the HREE, especially Lu. Mauna Loa is unreliable because of its jagged $\boldsymbol{D}_o^i$ profile and significantly larger error bars. No solution is possible for Mauna Loa unless the HREE boundary conditions, described below, are turned off. A provisional and controversial solution for Mauna Loa indicates an olivine websterite source and at least 50% melting. The shapes of $\boldsymbol{D}_o^i$ profiles change as C_o^{La} increases but most of the shape is inherited from the slope and intercept vectors. These are constants that make an intrinsic error level for the suite. The intrinsic error levels for the three suites in Figure 1d differ substantially. Mauna Kea's minimum D_{fit} error (Figure 9) is about 9×10^{-6}, Kiekie is higher (Figure 8) at about 8×10^{-5} and Mauna Loa is even higher at 1×10^{4}. The larger intrinsic error at Kiekie is likely caused by the high levels of garnet that lead to a large error in the HREE. This is not a problem that necessarily can be remedied by more or better data. The Mauna Loa intrinsic error is amenable to reduction by addition to the data set.

2.2. Partition Coefficients

Because Equation 13 compares bulk distribution coefficients from two different equations, small irregularities in partition coefficients might compromise the comparison. Therefore, experimental partition coefficients were adjusted to smooth parabolic shapes expected from theory (Onuma et al., 1968). We used the model developed by the Bristol group (Blundy & Wood, 2003) to select and, if necessary, slightly modify partition coefficients to approximate the theoretical shape. We assume simple sources containing olivine, orthopyroxene, clinopyroxene and garnet so our partition coefficients are limited to these minerals (Table 1). Spinel and other oxides with no affinity for the REEs may be occult in the olivine component. No provision was made for amphibole or phlogopite or any other mantle minerals.

2.3. Adjustments to D_o^i and C_o^i Required by the Assumption That $D^{La} = P^{La} = 0$

For any pair of melt and mantle modes, the effect of assuming perfect incompatibility for La can be calculated by making two synthetic batch melt models, a normal (n) suite of melts made with the partition coefficients for La and a zero (z) suite of melts made with the La partition coefficient at zero. For each model we make eight melts with different melt proportions and then make process identification regressions to determine S_n^i, I_n^i and S_z^i, I_z^i. The slope adjustment, S_a^i, is S_z^i/S_n^i and the intercept adjustment, I_a, is I_z^i/I_n^i. The intercept adjustment was empirically determined to be a constant whose value is approximately $1 + D^{La}–P^{La}$. Because clinopyroxene has the highest partition coefficient for La and is typically more abundant in a melt than in the mantle, I_a is usually between 0.99

and 0.96. The slope adjustments are large for the LREE but not highly variable. Average adjustments are the last columns of Table 1. In calculations using Equations 7, 8, and 10, S^i becomes $S^i_a S^i$ and I^i becomes $I_a I^i$.

The adjustments to slope and intercept are in the equation used to determine $\boldsymbol{D}^i_o$ which, in turn, is used to determine the mantle mode. However, the mantle mode is needed to determine the adjustments. Iterations address this circularity. An initial calculation uses the average adjustment in Table 1. If a mantle mode is successfully calculated using Equation 11, the adjustments are recalculated using the current melt mode and the estimated mantle mode. The mantle mode is then re-estimated, and the new adjustments replace the previous ones. The initial adjustments are satisfactory for the Mauna Kea suite, which has a small amount of garnet in the melt and mantle modes and moderate amounts of clinopyroxene. The submarine Kiekie suite has a much higher amount of garnet and low clinopyroxene. In this garnet-rich case, the initial adjustment failed until the melt mode search was centered on the correct garnet range.

3. Data Selection

To use this inverse method, magma suites should have REE patterns consistent with an origin by different degrees of batch melting of a uniform source. The HREE should be closer together than the LREE, creating a fan shape and opening to the left on a standard REE plot. Mixing of different sources is best recognized with radiogenic isotopic data. We accept some isotopic variation but reject any systematic stratigraphic changes indicating mixing. In Figure 2c, epsilon Nd increases up section for the low silica Mauna Kea group, making it suspect for REE modeling. Feigenson et al. (2003) showed that this group totally fails in the REE inverse model. Epsilon Nd for the high silica group has three outliers but otherwise does not vary up section. Although the high silica suite has wide dispersion in Nd isotopes, it allowed a REE inverse model (Feigenson et al., 2003), which we will refine in this work. The effects of accumulation and fractional crystallization are more reliably removed if olivine is the only fractionating mineral. Stratigraphic sequences, especially drill cores, are superior because they reveal relative time. Samples with Ce depletion and abnormally high HREE (Fodor et al., 1992) indicate weathering and must be ignored. The HSDP2 drill core is ideal because the high magma output rate buried flows before any obvious REE weathering occurred. The subaerial and submarine sections of the core have K and Rb variations consistent with leaching by fluids (Huang & Frey, 2003), but the REEs seem unaffected. The HSDP2 sample set, shared among several labs, includes 112 samples from Mauna Kea. Figure 2 shows selected analytical data (major elements, Rhodes & Vollinger, 2004; REE, Feigenson et al., 2003; and Nd isotopes, Bryce et al., 2005). The submarine section of the core allowed electron microprobe analyses of 512 fresh glasses (Stolper et al., 2004). This detailed section found complexities not seen in the less detailed sample set in Figure 2, but has no REE data.

The top of the Mauna Kea section has postshield lavas that are more alkalic than the rest, including one alkaline basalt (Huang & Frey, 2003; Rhodes & Vollinger, 2004). We did not attempt to make an inverse model for the postshield group. The rest of the Mauna Kea section sampled main stage tholeiites. The tholeiites separate into high-silica and low-silica types that are randomly interspersed in the stratigraphic section. The stratigraphic variation of MgO for the 66 high-silica samples (Figure 2b) is uniform with depth but there is wide dispersion. In contrast, the MgO content of the 28 low-silica samples evolves through the section but has lower dispersion over short intervals. The low-silica samples start near 15% MgO, which may be close to a primitive melt. Over time, MgO increases until near the top of the section where four low-silica samples are more fractionated and are akin to the late-stage lava. Initially, the low-silica samples have lower Nd isotopic ratios than the high-silica samples (Figure 2c), but higher in the section, their Nd isotopic ratios increase. In contrast, there is minimal stratigraphic variation in the Nd isotopes of the high-silica suite. Variation in La/Lu (Figure 2d) is random until a depth of about 1,000 m. The shallower samples of the low silica group have progressively higher La/Lu, culminating in an alkali basalt at the top of the Mauna Kea section.

The submarine Kiekie suite (Dixon et al., 2008) does not have the advantage of stratigraphic order. It does have excellent REE data that make the well-defined fan of REE profiles expected of variable degrees of batch melting (Figure 3b). We excluded T318-R19 which cut across the HREE profiles and T322-R6 which has an anomalously high Yb concentration after correction.

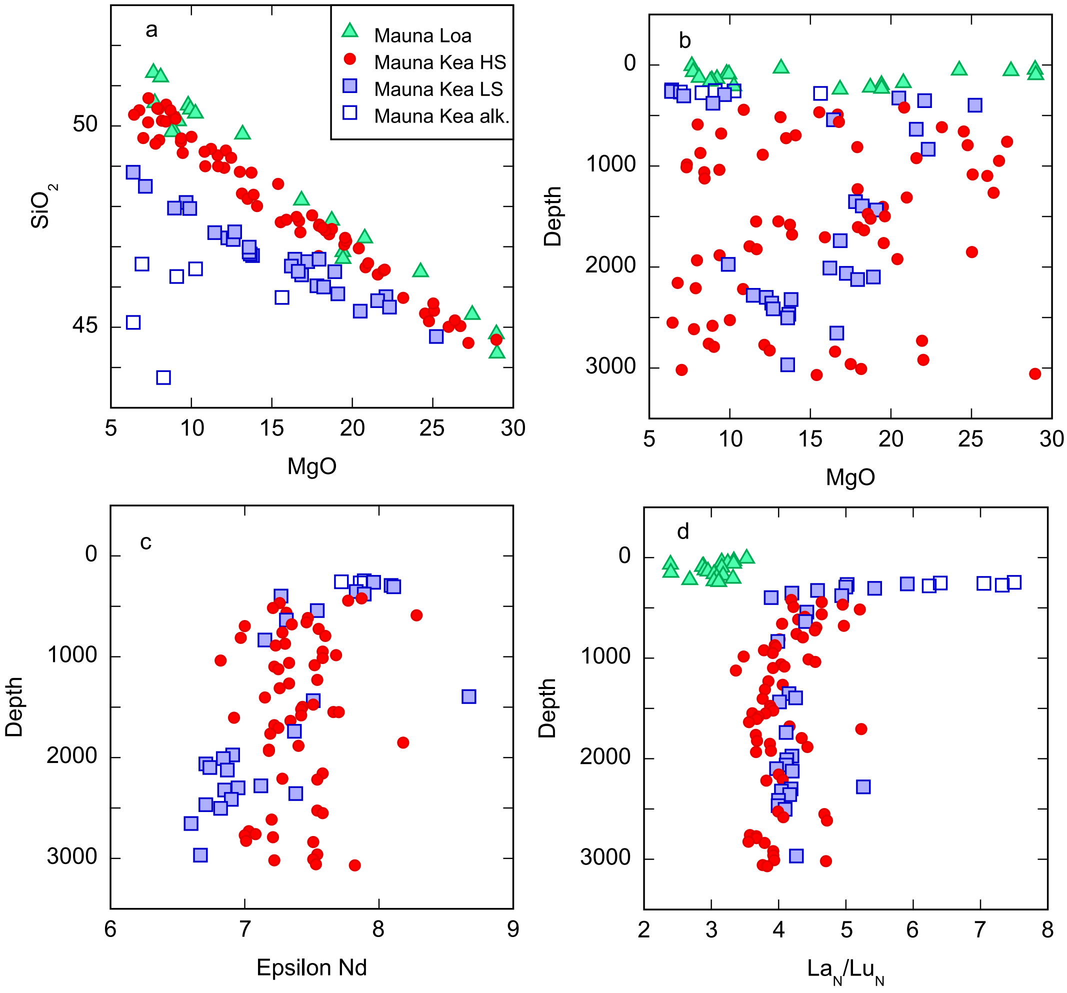

Figure 2. Characteristics of Hawaiian lava in the HSDP2 core. (a) Separation into groups. (b) Stratigraphic variation of MgO. (c) Stratigraphic variation of Nd isotopes. (d) Stratigraphic variation of La_N/Lu_N. Major elements from Rhodes and Vollinger (2004). Trace elements from Feigenson et al. (2003). Nd isotopic data from Bryce et al. (2005).

3.1. Correcting for Accumulation and Fractional Crystallization

To properly evaluate melting processes, REE concentrations must be corrected for the effects of fractional crystallization and crystal sorting. We first check whether a suite is on an olivine control line and Mauna Kea, Mauna Loa and submarine Kiekie are. The next step is to select a reference point to correct to. In our previous examination of the Mauna Kea section (Feigenson et al., 2003), we selected an arbitrary parent and used least squares to determine the olivine proportions to be added or subtracted to reach that parent. For this study, we chose to correct for a common Fo content for mantle olivine. Primelt3 (Herzberg & Asimow, 2015) adds and subtracts olivine to samples, calculates the resulting Fo of the olivine and tests whether the result is consistent with a melt of peridotite. Eight of the Kiekie samples returned primary magmas and ±olivine percentages. These primary melts are in equilibrium with olivines in a narrow range of Fo content with a mean of 91.1. We used that Fo content to estimate the amount of olivine addition needed for the remaining samples.

Primelt3 did not find any primary peridotite melts at Mauna Loa or Mauna Kea. To obtain reference Fo contents for these suites, we used Table 3 from Putirka et al. (2011), which has the following Fo_{max} values: Mauna Loa (91.3) and Mauna Kea (90.3). For each sample, we examined the Primelt3 up and down temperature calculations to locate the matching Fo and thus the ±olivine percentage needed to be in equilibrium with the appropriate Fo_{max}. Primelt3 allowed adjustment of 59 of the 66 samples from Mauna Kea. Seven samples with more than 25 wt% MgO had Fo values above 90.3 at all temperature steps and could not be used. Finally, we used the ± olivine

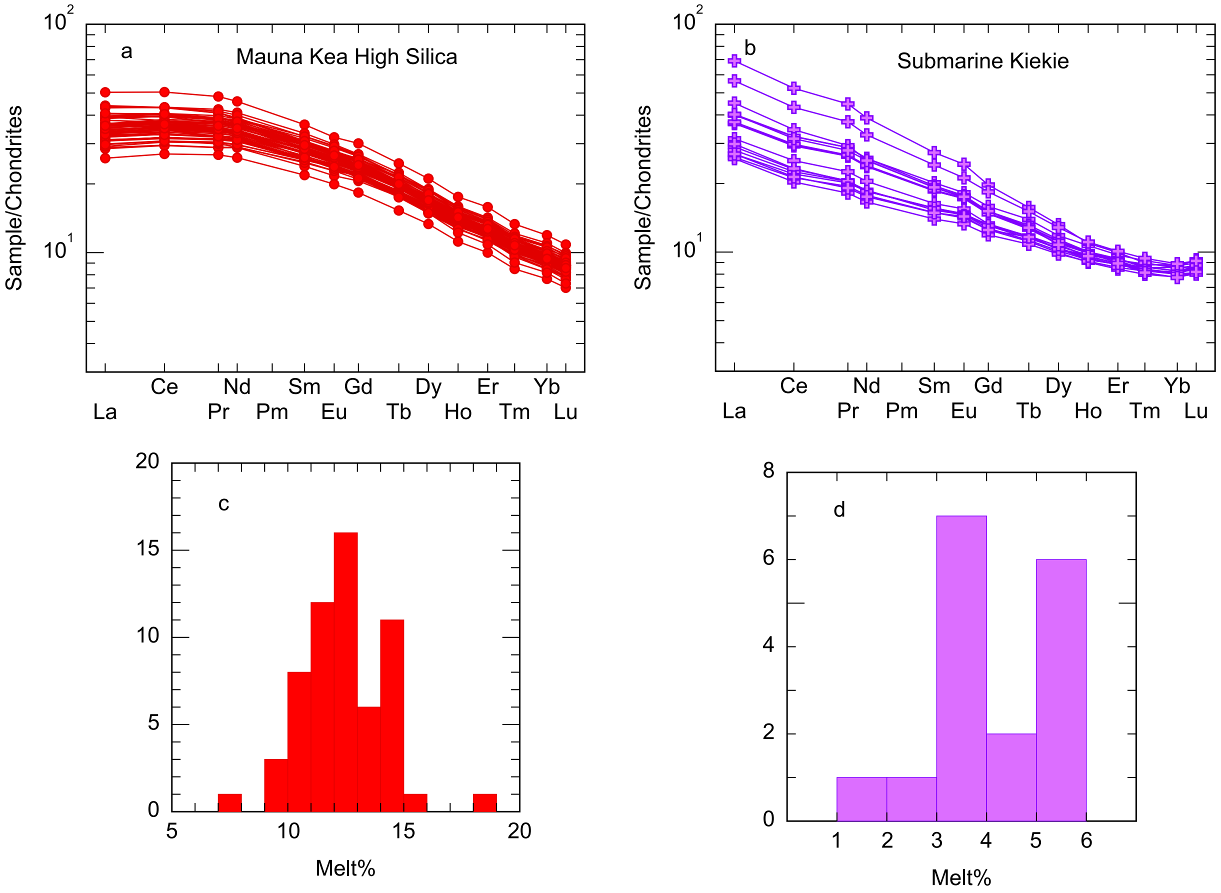

Figure 3. Corrected data for Hawaiian suites. (a) Mauna Kea High Silica. (b) Submarine Kiekie. (c) Mauna Kea melt% distribution for $C_o^{La} = 4.5$, $N = 59$, $\bar{x} = 12.5$, SD = 1.82. (d) Kiekie melt% distribution for $C_o^{La} = 1.5$, $N = 17$.

estimates, the partition coefficients for olivine, and the Rayleigh equation to correct the raw REE data for fractional crystallization and accumulation. The fractionation adjusted REE concentrations are in the Supplemental Table; Mauna Kea in Table S3 in Supporting Information S3; submarine Kiekie in Table S4 in Supporting Information S3; Mauna Loa in Table S5 in Supporting Information S3. The adjusted REE profile of Mauna Loa sample SR0046–1.15 has below average LREE and the highest HREE. Because it cuts across most other profiles, we ignored it. The S^i and I^i profiles for Mauna Loa have more noise than the Mauna Kea or submarine Kiekie profiles (Figure 1c) and we consider the resulting inverse model unreliable.

We made a preliminary model for a section of transitional lava from Mamaewa gulch on Kohala volcano (Feigenson et al., 1983). The Kohala samples have experienced clinopyroxene fractionation ruling out correction by Primelt3. Following Feigenson et al. (2003), we corrected for a likely parent composition using mass balance calculations. Some samples had odd REE profiles consistent with weathering and were excluded, leaving only eight samples. We decided not to proceed with the inverse model until the data set for Kohala is improved.

3.2. Contrasts of Mauna Kea and Submarine Kiekie

Main stage tholeiites from Mauna Kea and rejuvenated lavas from Niihau are fundamentally different (Figures 3a and 3b). The Mauna Kea REE profiles are subparallel, with only a small amount of widening at the LREE end. In contrast, the submarine Kiekie REE profiles are close together in the HREE and widen substantially in the LREE. Process identification diagrams transform the information in Figures 3a and 3b into S^i and I^i vectors (Figure 1c). Linear regressions that define the S^i and I^i vectors provide standard error statistics that allow calculation of error bars in Figure 1c and several subsequent figures. Note that Lu for Kiekie has an intercept below 0.25 in Figure 1c.

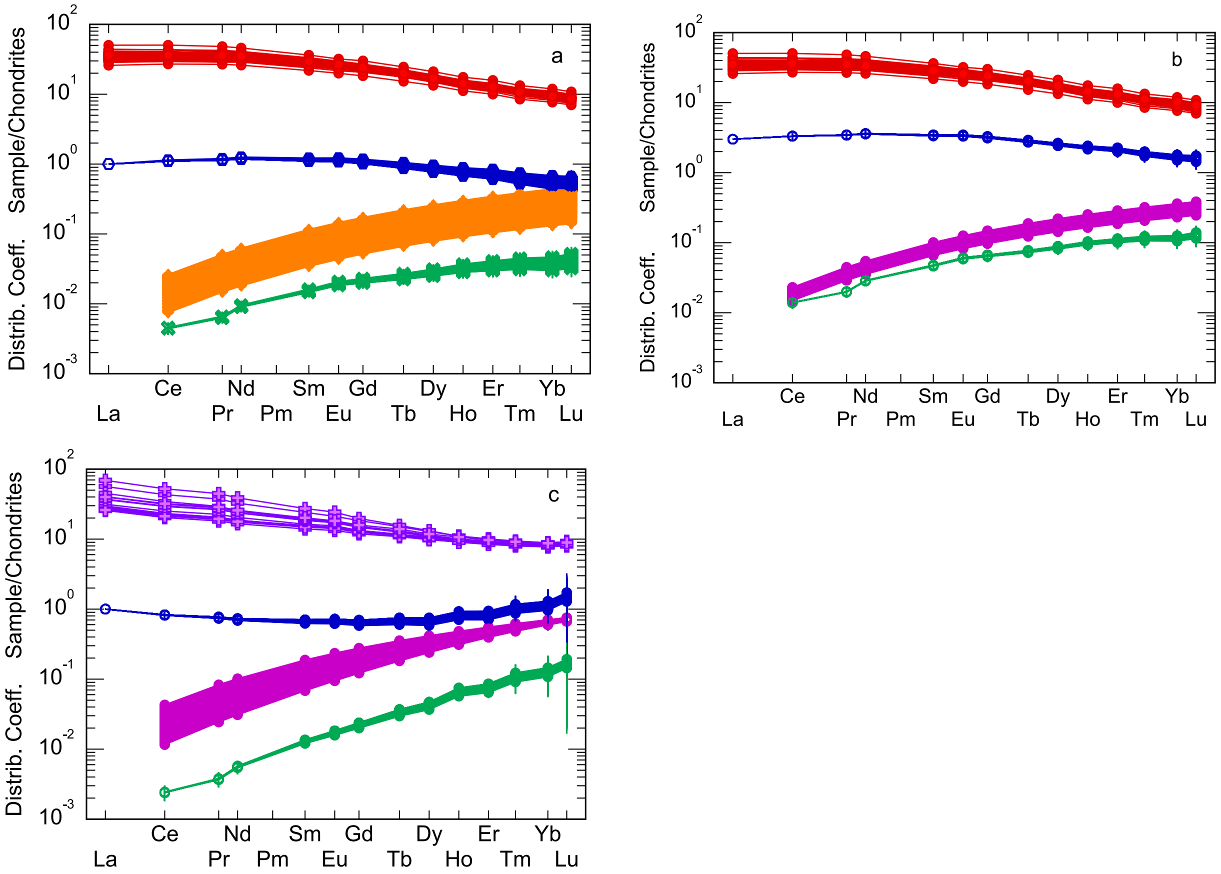

Figure 4. C_o^i D_o^i P^i models for Mauna Kea and submarine Kiekie. In each case, lava profiles are at the top, followed by C_o^i, then P^i, then D_o^i. (a) Mauna Kea at $C_o^{La} = 1$. Lavas are red; C_o^i profiles are blue; and D_o^i are green. Because all 2,529 trials fail, the P^i field is orange. (b) Mauna Kea at $C_o^{La} = 3$. P^i are magenta because only the 528 trials that pass all boundary conditions are plotted. (c) Kiekie at $C_o^{La} = 1$. Lavas are purple. The 693 viable melt mode trials indicate a more depleted source for Kiekie.

Because the intercept is in the denominator in Equations 7 and 8, Lu is automatically given a weight of zero because intercepts near zero cause exaggerated noise, as indicated by the large error bar for Lu in Figures 1c and 1d.

Using Equation 10, estimates of C_o^{La} convert the REE profiles to melt percentages for Mauna Kea (Figure 3c) and Kiekie (Figure 3d). The reliability of the C_o^{La} estimates is discussed below. The melt percentages for Mauna Kea have a normal distribution with a maximum of 18.7%. The distribution for Kiekie is not clear but looks skewed with 6 of the 17 samples in the highest bin between 5% and 6%. There is almost no overlap between the two suites. We designate the sample with the highest melt percentage (or lowest REE profile) as the basal sample. For Mauna Kea this is sample SR0622–7.10. The basal sample for Kiekie is T318-R11. The melt proportion of the basal sample is determined using Equation 10 and the current C_o^{La} value and used in the maximum melt boundary condition described below.

4. Structure of the Inverse

Feigenson et al. (2003) made fixed C_o^i D_o^i P^i models assuming that C_o^{La} equals 1.0. These qualitative models use the field of input $\boldsymbol{P}^i$ and Equations 7 and 8 to define fields for source (C_o^i) and bulk distribution coefficient ($\boldsymbol{D}_o^i$). At Mauna Kea (Figure 4a) all 2,529 trials fail because the $\boldsymbol{D}_o^i$ profiles are so low that solving Equation 11 for the estimated mantle mode, d^j, results in a negative proportion for garnet. A negative mineral proportion means a trial fails. In contrast, 693 trials passed all the boundary conditions in Table 2 for the Kiekie model, indicating a more depleted source (Figure 4c). By assigning a different value to C_o^{La} we raise or lower C_o^i and $\boldsymbol{D}_o^i$ relative to $\boldsymbol{P}^i$, which lacks a C_o^{La} term. Note the differences between Figures 4a and 4b. At $C_o^{La} = 3.0$, 528 melt mode trials pass all the

Table 2
Boundary Conditions

#	Description	Utility	Remarks
	Independent of C_o^{La}		
1	Maximum % olivine in the melt	Very important	20%
2	HREE ratio (too high or too low)	Very important	Table 3
3	Source vector hits base of REE data	Not used	
4	Maximum % garnet in mantle <15%	Advisory	15
	Varies with C_o^{La}		
5	Mantle modes (all positive)	Very important	Equation 11
6	Maximum melt (must be below)	Most important	Figure 5d
7	D > P (fail)	Important	
8	$D^{Ce} > P^{Ce}$ (fail)	Useful	
	Applied after Traverse run		
9	Pol edge effect	Important	

boundary conditions, whereas at $C_o^{La} = 1.0$, no trials pass. The centers of the $\boldsymbol{P}^i$ fields in Figures 4a and 4b are the same, but the C_o^i and $\boldsymbol{D}_o^i$ fields differ by C_o^{La}, a factor of 3.0. If C_o^{La} is systematically incremented with small steps, many "Fixed" models combine into a "Traverse."

The new C_o^i D_o^i P^i model has three options, Fixed, Traverse and Traverse plus. The Fixed option runs at a selected value of C_o^{La} and calculates D_{fit}, the melt mode, the mantle mode, $\boldsymbol{P}^i$, C_o^i, $\boldsymbol{D}_o^i$, $\boldsymbol{D}_c^i$, and related parameters for a grid of trial melt modes. All the grid points are put into pass/fail categories and stored so the model can be examined. The main purpose of the Fixed option is to locate the minimum valid D_{fit} at the selected value of C_o^{La}, where valid means the trial passed all the boundary conditions. The secondary purpose is to allow visualization of the boundary conditions and their effects. The Traverse option steps through a range of C_o^{La} and saves the simplified results of 50 or more Fixed searches, keeping only the main parameters of the minimum valid D_{fit} for each step. The purpose of a traverse is to define an inverse path through mantle mode and melt mode space (Figure 8). Traverse runs are long and generate small files. Fixed runs are short but make very large files. Traverse Plus provides the simple traverse output and the detailed fixed output for a few selected values of C_o^{La}. This simplifies extracting the final $\boldsymbol{P}^i$, C_o^i, $\boldsymbol{D}_o^i$, $\boldsymbol{D}_c^i$ profiles.

Most of the inverse calculations are in the Fixed section of C_o^i D_o^i P^i (Figure 5). The operations in the flow chart before the three melt mode loops are interactive. The selection of an S&I file refers to the slope and intercept statistics from process identification diagrams. These files are made from corrected REE data in a different section of Igpet (Feigenson et al., 2003). A traverse flow chart would select the Traverse option and have an additional loop connecting a range of C_o^{La} to the last operation. The SA inside a circle is the subroutine described in Section 2.3.

The procedures within the loop test and classify the melt mode trials. The first step, calculation of C_o^i and $\boldsymbol{D}_o^i$, is straightforward. The next four procedures test boundary conditions (Table 2 and Section 5). The Mantle mode test (#5) is where a golden section optimization selects a Dol# for the mantle mode. This is a time-consuming iterative procedure. Many trials fail here by generating negative garnet or negative clinopyroxene.

The three dimensions of the input melt mode grid are Pgt, Pcpx and Pol#. For reconnaissance, we set the base of the grid at 0%–40% Pcpx and 0%–15% Pgt (Figure 6a). The Pol# range is typically 0 to 40 (Figure 6b). The mafic sum (Pol + Popx) is 100%-Pgt-Pcpx. The Pol# loop apportions the mafic sum to Pol and Popx. Each grid point is classified as pass or fail and the fails are detailed (legend in 6a). The ranges and steps can be adjusted to show more detail or a wider scope, but the ranges should extend beyond the region where valid trials occur. We adjust ranges by trial and error.

A coarsely spaced grid for Mauna Kea at $C_o^{La} = 3$ shows regular D_{fit} variations through the melt mode loops. Pgt is the outermost loop and the variation of D_{fit} with Pgt is simple (Figure 6c). Figure 6d shows all three melt mode loops; the Pgt steps become arcuate bands of short vertical lines that are the Pol# ranges. The boundary conditions isolate the passing trials into a small volume in Pcpx-Pgt space. The ordering by D_{fit} narrows the choice, favoring Pgt = 3 and Pcpx of about 15.

5. Boundary Conditions

Feigenson et al. (2003) made no assumptions about melt modes and used Monte Carlo testing to define the field of acceptable $\boldsymbol{D}_o^i$ profiles. They used two boundary conditions; $\boldsymbol{P}^i$ must be less than one if all intercepts are positive, and the shape of $\boldsymbol{P}^i$ must bear some resemblance to $\boldsymbol{D}_o^i$ because the minerals that enter the melt must have been initially present in the source. We get the same result (Figure 4a) with four boundary conditions that are independent of C_o^{La} and apply equally to all steps in a traverse. We recognize five additional boundary conditions that vary with C_o^{La} (Table 2).

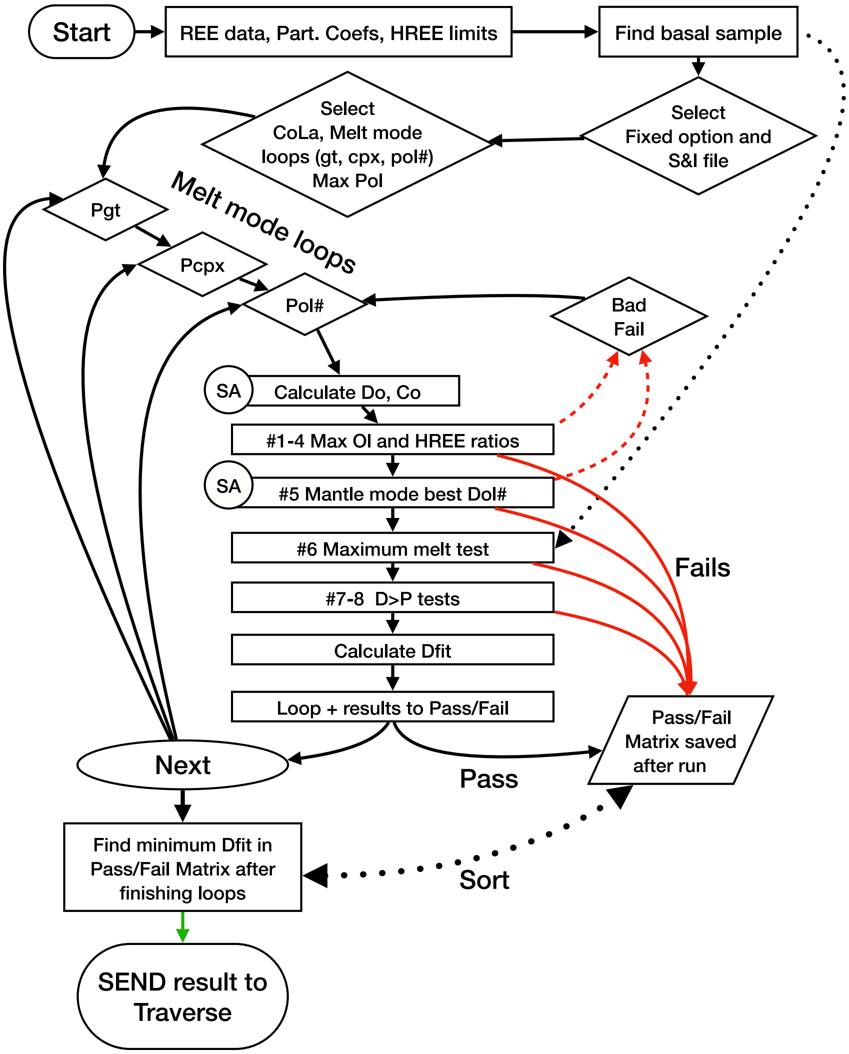

Figure 5. Flow Chart of a Fixed mode run. Dashed red flowlines are critical failures that prevent the calculation of mantle modes. Flow lines lead to classification and storage in the Pass/Fail matrix. The SA subroutine corrects S^i for the assumption that the partition coefficient for La is zero. A basal sample is needed for the maximum melt test.

5.1. Boundary Conditions Independent of C_o^{La}

The first boundary condition is the maximum % olivine allowed in the melt mode. A melt mode with 3% gt and 7% cpx will have 90% ol + opx, most likely leading to an unreasonably high olivine proportion in the melt mode. Mauna Kea lavas have estimated primary magmas that range up to 19% MgO, which implies no more than about 20% olivine in the melt mode. At shallow depths of melting, spinel replaces garnet as the mantle's aluminous phase and because spinel has minimal affinity for the REE, it can be included with olivine, increasing the olivine-like component. Although the best petrologic choice for an olivine limit is not clear, a 20% limit is a reasonable choice.

The first two boundary conditions eliminate large volumes of the melt mode grid (Figures 6a and 6b) The olivine limit of 20% translates into a diagonal boundary in Figure 6b because, as Pcpx increases, the Pol# proportion can be higher because the Pol + Popx sum is lower. Note that the field of excess olivine failure has only one contact with the purple field of melt modes that pass all the boundary conditions, so the lack of rigor in the olivine limit may not be important. Figure 6a looks at the Pol# = 30 level near the top of the Pol# range with successful trials. The effect of the first two boundary conditions is to put black symbols on most of this section. The excess olivine test is performed first so that the symbol dominates. The second boundary condition is HREE ratio failure, either

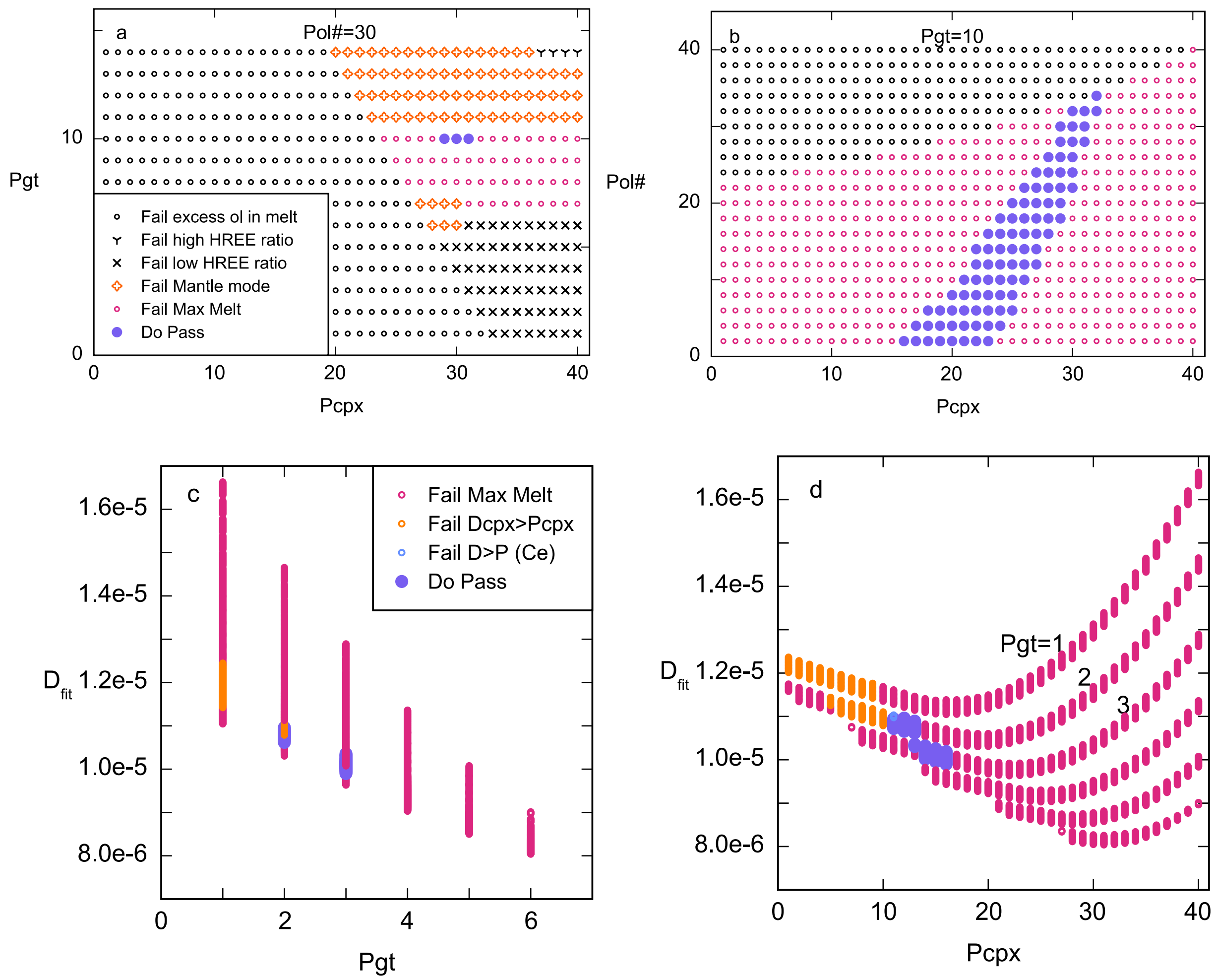

Figure 6. Structure of inverse and sorting by D_{fit}. (a) Base of melt mode grid for Kiekie at $C_o^{La} = 1$ and Pol# = 30. Black symbols are rejected melt modes. Most fail for excess olivine in the melt but some fail for low or high HREE ratios. (b) Vertical section of Kiekie melt mode grid at Pgt = 10. Symbols as in a. About a third of the grid is rejected for having excess olivine in the melt. (c) A coarse Mauna Kea melt mode grid at $C_o^{La} = 3.0$ ordered by D_{fit}. Pgt is the outermost grid loop. (d) Same grid and symbols as in c. The first three Pgt loops are labeled. The Pol# loops make the vertical bars in the Pgt loops.

too high or too low. Low failures extend from the base up to 6% Pgt (Figure 6a). Three successful trials in purple are surrounded by brighter colors marking failures in tests that vary with C_o^{La}. The zoning of failure classes surrounding successful trials makes it likely that no successful trials are wrongly cut off.

We eliminate melt modes with impossible HREE ratios in $\boldsymbol{D}_o^i$ profiles. In the Kiekie case, most of the HREE failures are too low (x symbol in Figure 6a). At Mauna Kea (Figure 7a), melt modes fail because the HREE ratios are too high. Ratios of bulk distribution coefficients calculated from mantle modes must stay within the bounds allowed by the partition coefficients of the mantle minerals. However, $\boldsymbol{D}_o^i$ profiles, calculated from Equation 8, are not constrained. Depending upon the values of S^i, I^i, and $\boldsymbol{P}^i$, the HREE end of a $\boldsymbol{D}_o^i$ profile may bend sharply up or down. We selected three HREE ratios to screen for impossible $\boldsymbol{D}_o^i$ profiles. If a $\boldsymbol{D}_o^i$ profile has ratios outside the bounds selected, that melt mode is failed. The black field in Figure 7a shows many completely unrealistic $\boldsymbol{D}_o^i$ profiles calculated from Equation 8. The green X field in Figure 7a is the same as the $\boldsymbol{D}_o^i$ field in Figure 4a. Two HREE ratio limits are useful (Table 3). The "No limits" choice ignores this test. "Max range," based on the ratios for clinopyroxene for the upper limits and olivine for the lower limits, is the safe choice. This wide window allows some unpromising trials to continue, but later tests will eliminate them. Final models are focused on limited ranges of garnet and clinopyroxene that yield successful estimates of mantle modes; therefore, the HREE limits

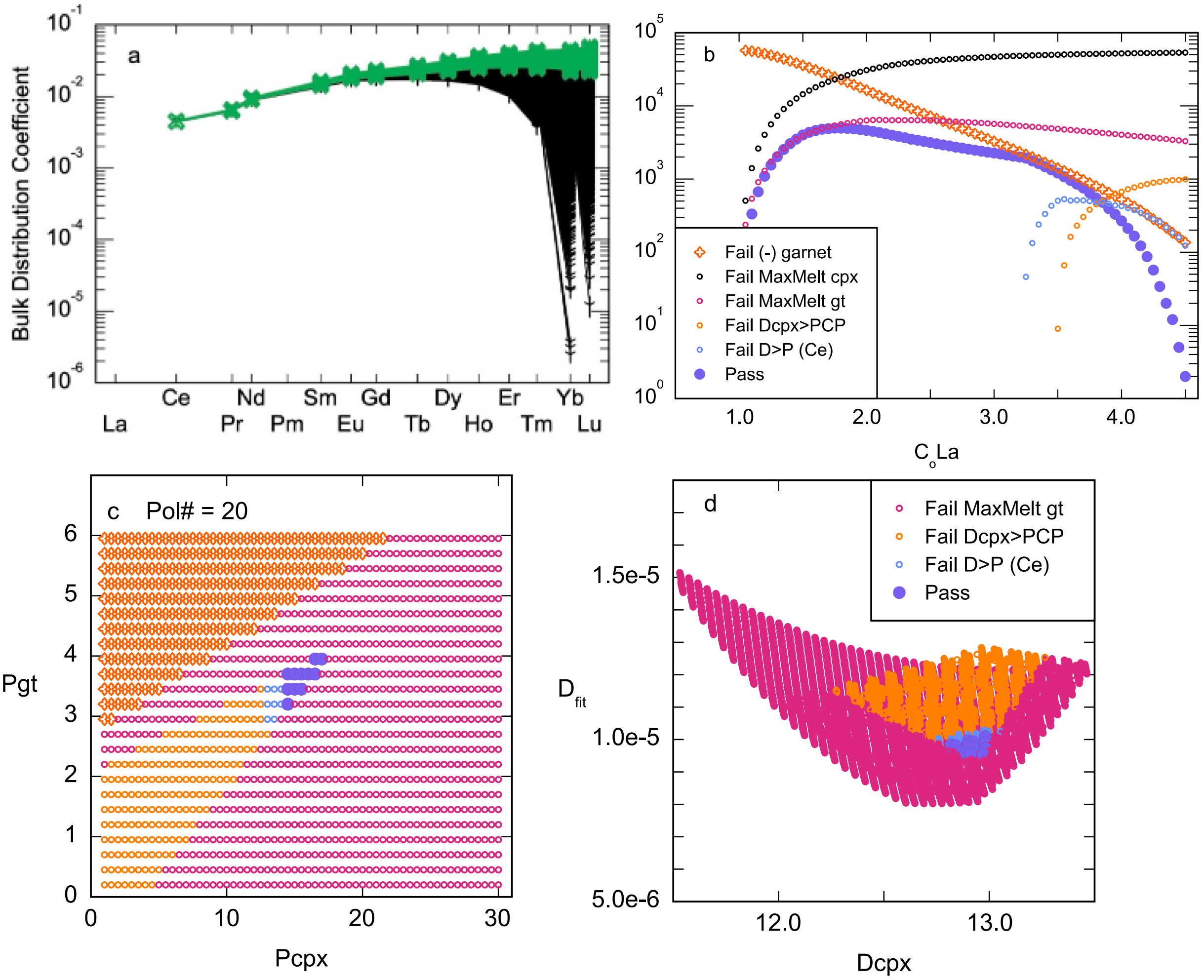

Figure 7. Effects of boundary conditions on Mauna Kea model. (a) D_o^i profiles for Mauna Kea with $C_o^{La} = 1$. Black Y profiles fail for high HREE ratios. Green X profiles, also plotted in 4a, have negative garnet in the estimated mantle mode. (b) Monitoring the fate of melt mode trials along the Mauna Kea traverse. (c) Mauna Kea at $C_o^{La} = 3.8$. All Pol# levels projected to the base. (d) Mauna Kea at $C_o^{La} = 3.8$. D_{fit} versus mantle clinopyroxene. 95 trials that passed all tests clustered near 12.9%Dcpx.

eliminate rather few melt mode trials at that stage. This is not the case at the beginning of a search when the melt mode ranges are wide.

The third boundary condition eliminates trials if $C_o^{La} \times C_o^{HREE}$ extends into the base of the lava field. HREE includes Dy, Er, Yb, Lu. At high values of C_o^{La}, the C_o^i profile may rise into the field of the actual data. This may be acceptable if there is considerable garnet in the mantle, but, at present, this test will eliminate trials when they intersect the field of actual data. With the Hawaiian suites, this test has not failed any melt mode trials.

Table 3
Limits on HREE Ratios

	Yb/Lu		Dy/Er		Er/Yb	
Limit	Min	Max	Min	Max	Min	Max
Max Range	0.80	1.07	0.44	0.99	0.47	1.14
Cpx alone		1.07		0.99		1.14
Olivine alone	0.80		0.44		0.47	
No Limit	0.00	2.00	0.00	2.00	0.00	2.00

The fourth boundary condition is a cautionary upper limit for garnet in the melt mode. It is based on the observation that crossing patterns are infrequent in lava suites that have uniform isotopic compositions and are restricted in space and time. However, Garcia et al. (2010) found crossing patterns in lava from Kaua'i, so this is not an absolute limit. In batch melting and aggregated fractional melting, the condition that leads to crossing patterns is $\boldsymbol{P}^i > 1$. Dy and heavier REEs have the potential to have $\boldsymbol{P}^i > 1$, but Lu, with the largest partition coefficient for garnet, is the most likely. For an eclogitic melt with no olivine or orthopyroxene, the limit of garnet in the melt is about 10%. A somewhat unrealistic melt of just garnet, olivine and orthopyroxene allows up to 20% garnet. As a rule of thumb, we suggest an upper limit of 15% on garnet

Table 4
Summary of Mauna Kea and Kiekie Models

				Melt mode				Mantle mode					%F	%F
Suite	Xol#	Tol.	C_o^{La}	Pgt	Pcpx	Pol	Popx	Dgt	Dcpx	Dol	Dopx	Dol#	min	Max
Mauna Kea (preferred)	100	0.5	4.50	4.4	17.5	17.2	60.9	0.85	15.4	71.9	11.9	85.8	7.06	19.0
Mauna Kea	90	1.0	4.50	4.4	17.5	17.2	60.9	0.85	15.4	72.0	11.8	85.9	7.04	19.0
Mauna Kea	85	1.0	5.25	4.5	20.8	16.4	58.3	1.00	17.6	68.5	13.0	84.1	8.21	22.2
Mauna Kea	80	1.0	5.30	4.2	20.5	3.0	72.3	0.94	17.5	64.5	17.0	79.1	8.31	22.4
Synthetic 1.31	100	0.5	5.00	4.4	15.8	11.2	68.6	0.93	15.7	68.6	14.7	82.4	4.78	21.2
Kiekie	100	0.5	1.0	9.5	37.4	3.72	49.4	1.81	1.44	94.6	2.15	97.8	1.34	3.86
Kiekie	100	0.5	1.5	9.6	37.2	2.39	50.8	2.86	2.15	91.8	3.18	96.7	2.01	5.78
Kiekie (preferred)	100	0.5	2.0	9.7	37.0	0.53	52.8	3.91	2.86	88.9	4.35	95.3	2.68	7.70
Refractory mantle (Dixon et al., 2008)			na	na	na	na	na	3.00	11.00	80.0	6.00	93.0	7.06	19.0

in the melt mode. In synthetic models made without error, the inverse handled melt modes with garnet as high as 35%. However, high garnet proportions also lead to intercepts near zero, which causes the affected HREE to be very noisy. The garnet upper limit is an input and there is no need for a runtime test. Furthermore, high values of garnet in the melt mode will likely cause failure in the HREE ratio limits.

5.2. Boundary Conditions That Vary With C_o^{La}

Boundary conditions that vary with C_o^{La} are essential for defining the inverse path through mantle mode and melt mode space. The first four boundary conditions remove seriously flawed $\boldsymbol{D}_o^i$ profiles. The final Mauna Kea traverse had 79,135 trial melt modes for each C_o^{La} step and lost 21,062 to the initial tests. The effects of the remaining boundary conditions vary strongly with C_o^{La} (Figure 7b). For Mauna Kea the number of successful melt mode trials (purple in Figure 7b) is six at $C_o^{La} = 1.0$ and two at $C_o^{La} = 4.5$. Between these end points, the number of successes reaches a maximum of 4,956. At $C_o^{La} = 1.0$ most of the 58,073 remaining trials fail the mantle mode test (#5) by generating negative garnet in Equation 11. As C_o^{La} increases, the mantle mode test fails fewer trials but the maximum melt test (#6) fails more. Tests 7 and 8 begin to have effects at $C_o^{La} > 3.25$ as the $\boldsymbol{D}_o^i$ profiles rise into the field of P^i profiles.

The mantle mode test (#5) checks a condition that the remaining tests require. Does the mantle mode generated by solving Equation 11 have all positive mineral proportions? Estimating a valid mantle mode changes the model from a qualitative answer (shapes) to a quantitative one. We combined olivine and orthopyroxene into a mafic composite for Equation 11 because not doing so commonly resulted in offsetting positive and negative proportions, usually greater than 100%. A small amount of incongruent melting for olivine might be reasonable, but we ignored that complication. Clinopyroxene and garnet can have invalid negative proportions and many trials generate negative garnet at Mauna Kea. This is not surprising given that the mantle garnet proportions obtained for Mauna Kea are less than 2%. Trials that fail this test are orange crosses in the upper left corner of Figure 7c. The Mauna Kea model tolerates up to 4.5% garnet (Pgt) in the melt but much less in the mantle (Table 4).

The next boundary condition, a maximum melt test (#6), determines if the melt and mantle mineral proportions will allow a high enough degree of melting to match the base of the data array. The melt proportion, F^i, of the sample at the base of the data array is determined using Equation 10 and the current C_o^{La} value. F^i is proportional to C_o^{La} as the other terms in Equation 10 are fixed. The maximum melt% that can be extracted at an invariant point until one mineral is gone is estimated from the melt and mantle modes using the lever rule for each mineral. If the melt proportion calculated for the base is less than the maximum melt allowed, then the trial passes. This simplification of melting solved a problem common in preliminary results, the inability of models over-relying on minimizing D_{fit} to replicate the base of the input REE profiles. The maximum melt test in Figures 7c and 7d eliminates a great many trials whose D_{fit} values are lower than the eventually selected minimum D_{fit}. Prior to adding this condition, most models failed to reproduce the base of the data. Figure 7d conclusively shows that D_{fit}, by itself, is inadequate for locating the best valid fit. Figure 7b shows that the maximum melt test is the boundary condition that eliminates most trials.

The sample at the base of the Mauna Kea array is SRO622–7.10 with an estimated 18.7% melt at $C_o^{La} = 4.5$. Because the maximum melt test is tied to the basal sample, 4.5 is the maximum. If a new sample is found with a lower REE profile (requiring a higher % melt), a revised inverse will find a lower value for C_o^{La}. Using several synthetic suites, we determined that the slope, $\Delta F_{max}/\Delta C_o^{La}$, is about −3. To lower C_o^{La} for Mauna Kea by 1 unit, a new sample will have to have 21.7% melt. For Mauna Kea, this is unlikely because the base melt, SRO622–7.10, is already 3.4 standard deviations above the mean of a normal distribution (Figure 3c).

Adding the maximum melt restriction to Figure 7c leaves just a wedge of remaining possible successes. The seventh and eighth tests compare the $\boldsymbol{D}_o^i$ profile to the $\boldsymbol{P}^i$ profile. We assert that the bulk distribution coefficient of the melt should always be greater than the bulk distribution coefficient of the mantle. Eventually, the $\boldsymbol{D}_o^i$ profile will rise above the $\boldsymbol{P}^i$ profile because as increasing C_o^{La} raises the $\boldsymbol{D}^i$ profile, the $\boldsymbol{P}^i$ profile moves only by changing the melt mode, specifically by losing Pol and gaining Pgt, Pcpx, and Popx. We want to remove all trials where $\boldsymbol{D}^i > \boldsymbol{P}^i$, but these two vectors are not generally parallel, so we use two tests. The first, test (#7), compares the clinopyroxene proportions for the mantle and melt and Dcpx > Pcpx fails. The bulk distribution coefficients are strongly influenced by garnet and clinopyroxene and clinopyroxene usually has a higher mantle mode; thus, the focus is on clinopyroxene. Most of the remaining wedges of trials, those with Pcpx < 14.5 in Figure 7c, fail this test. Failures are the gold regions in Figures 7c and 7d. Note that clinopyroxene dominance is not true for Kiekie. However, the clinopyroxene based test is insignificant for Kiekie because of the large separation between $\boldsymbol{D}^i$ and $\boldsymbol{P}^i$ (Figure 4c) and the low estimates of C_o^{La}.

We also fail trials if $\boldsymbol{D}_o^{Ce} < \boldsymbol{P}^{Ce}$. This test (#8) is a more stringent comparison of the $\boldsymbol{D}_o^i$ and $\boldsymbol{P}^i$ profiles. It may create a bias against higher values of C_o^{La}. Therefore, there is an option to turn off this test. Only a few points (blue) fail this test in Figures 7c and 7d. If we run the inverse for Mauna Kea with this test turned off, the value obtained for C_o^{La} increases from 4.5 to 4.9. The first eight boundary conditions greatly reduce the field of possible solutions (e.g., purple in Figure 7d). To select the single closest fit for this C_o^{La} step now requires comparing the relatively few (41) survivors in Figure 7d to find the one that has the lowest D_{fit}.

5.3. Two Interventions

Eight boundary conditions are applied algorithmically, but two additional interventions are useful. The first is to eliminate a possible Pol edge effect caused by the first boundary condition, the limit on olivine in the melt to 20% or less. C_o^{La} steps that would have had Pol >20% cluster around 19% Pol, creating a distortion of melt and mantle mode mineral proportions. Similarly, Pol values can cluster around the lower limit, usually zero. Similar edge effects occur if the trial ranges for Pgt or Pcpx are too narrow, but in these cases the remedy is to run the traverse again with a wider range. The Pol edge effect is an additional boundary condition applied after a traverse run. It is necessary in deliberately perturbed traverses for Mauna Kea (Figure 9). The valid Pol range for Mauna Kea ($2 < \text{Pol} < 18.5$) was set by examination of Figure 9b. In Figures 9c and 9e, we eliminated the steps outside the Pol range because the distortions of the perturbed traverses were large. Distortions appear to be less important with unperturbed traverses. Therefore, in Figures 8 and 10, we keep the steps outside the valid Pol range but show them with a small open symbol.

The second intervention is an arbitrary restraint on the relative proportions of olivine and orthopyroxene. We doubted that the golden section method for optimizing the Dol# would be effective, so we added a maximum setting, Xol#. By setting Xol# to less than 100, the Dopx proportion increases at the expense of Dol and the model is perturbed until C_o^{La} is high enough to generate a Dol# less than the maximum setting. We used maximum Xol# values of 100 (or normal), 90, 85, and 80 with the intent of creating a petrogenetic grid for Mauna Kea. Instead, we created a perturbation that was useful for Mauna Kea (Figure 9) but not at Kiekie.

6. Inverse Paths Through Mantle and Melt Mode Space

$\boldsymbol{D}_o^i$ can be calculated for any melt mode but most $\boldsymbol{D}_o^i$ profiles have flaws, ranging from gross distortions to subtle inconsistencies. The boundary conditions that rule out melt mode trials have the surprising effect of generating coherent paths through melt mode and mantle mode space. Even olivine and orthopyroxene have some systematic

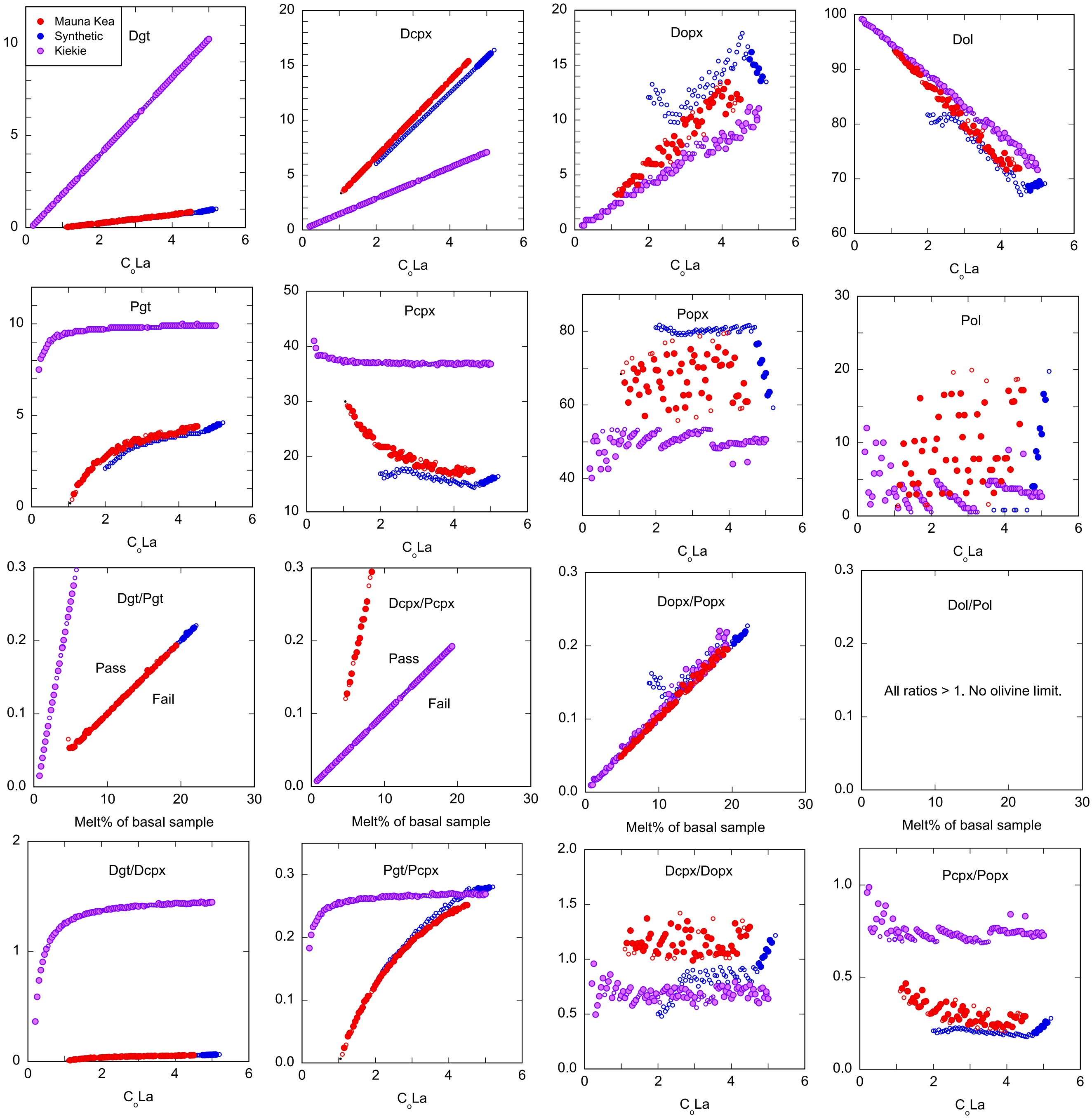

Figure 8. Inverse paths of mantle and melt modes for Hawaiian suites. Red steps from the normal Mauna Kea traverse. Purple steps from the Kiekie traverse. Dark blue steps from the synthetic melt traverse. Open symbols are less reliable because of Pol edge effects. Top row is mantle mode. Second row is melt mode. Third row is maximum melt test where the *x*-axis is melt % needed to fit the basal sample and *y*-axis is melt proportion allowed. The maximum melt test causes the 45° lines separating passing and failing trials. Fourth row suggests that Kiekie has limiting ratios in the mantle and melt modes.

behavior. Systematic mantle mode variations are expected from Equation 8, but systematic behavior by the melt modes is caused by boundary conditions that select the optimum surviving melt mode at each C_o^{La} step. Inverse paths (Figure 8) show how melt and mantle modes change as C_o^{La} increases. Inverse paths are not liquid lines of descent or phase boudaries but progressions of potential solutions controlled by the interacton of the $\boldsymbol{D}_o^i$ equation, the boundary conditions and D_{fit}. The systematics shown in Figure 8 show the variation in the number of successful melt mode trials (e.g., Figure 7b) and the variation in D_{fit} along C_o^{La} traverses (Figures 9 and 10) allow

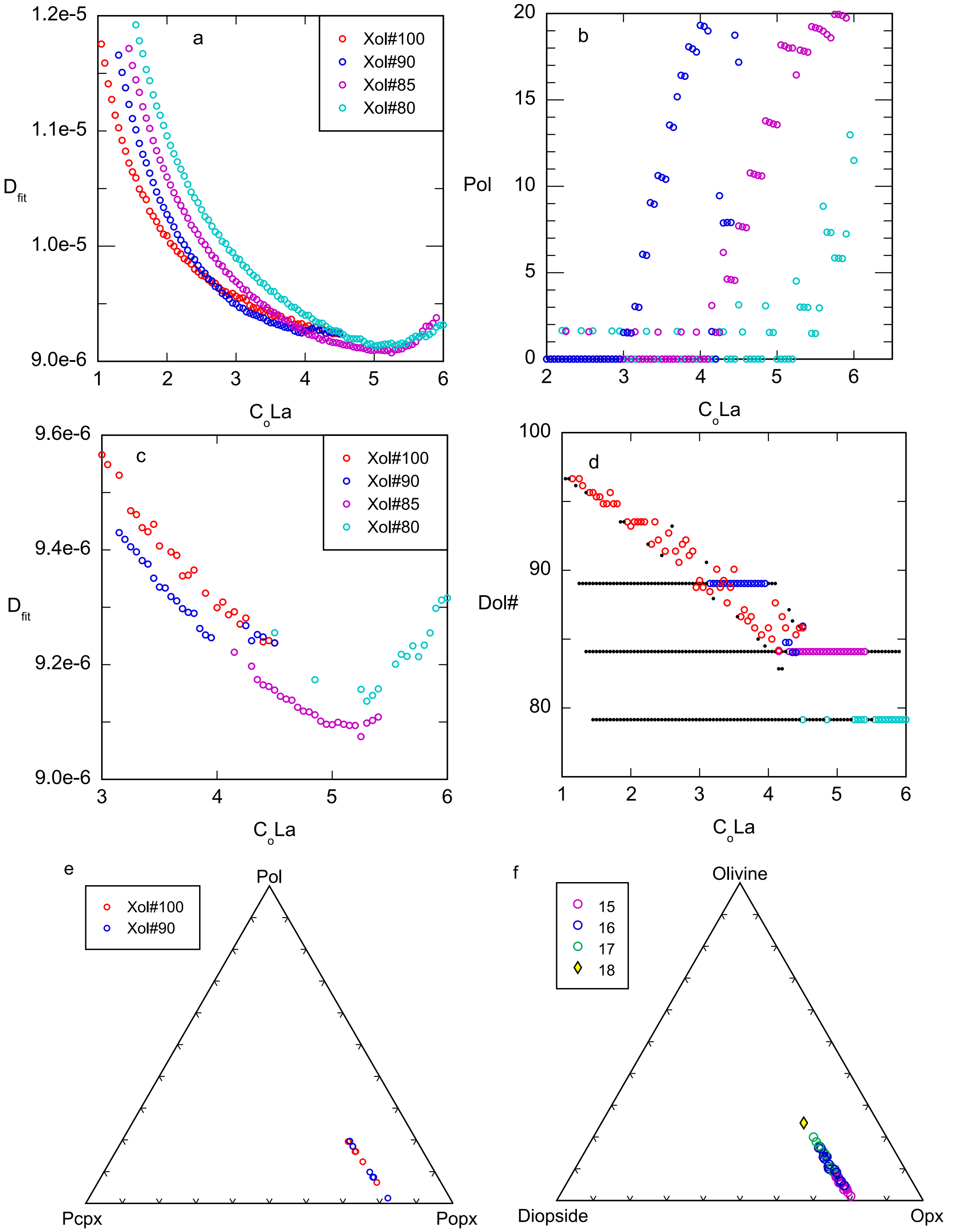

Figure 9. Locating C_o^{La} for Mauna Kea. (a) C_o^{La} traverses with varying levels of Dol# restriction. Pol limits ignored. (b) Pol versus C_o^{La} for. Pol values below 2 and above 18.5 are edge effects. (c) Consolidated C_o^{La} traverse includes only steps unaffected by the Pol edge effect. (d) Dol# versus C_o^{La}. Steps outside the Pol limits (black dots) are failures. (e) Projection of traverse steps into melt mode space. Compare to f. All steps affected by Xol# limits or by Pol edge effects are removed. The 15 steps plotted have $C_o^{La} > 4.1$. (f) Mauna Kea samples in anorthite projection with oxides assigned to CMAS following Herzberg and O'Hara (1998). MgO range 15.5–18.5. Compare f to e.

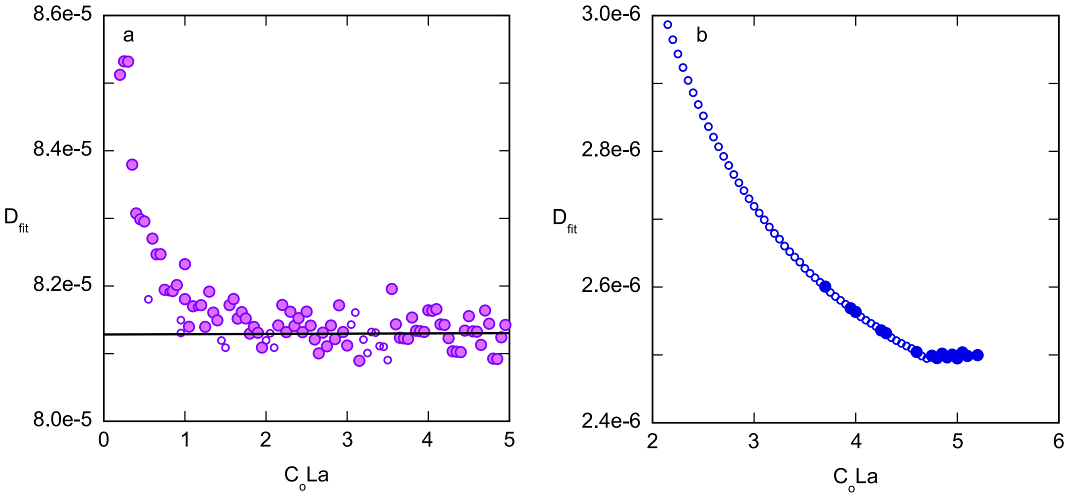

Figure 10. C_o^{La} choices for Kiekie and synthetic Mauna Kea. (a) Kiekie traverse with regression line for D_{fit} versus C_o^{La} calculated between 2.5 and 5. Small open symbols have Pol values outside the allowed range and are less reliable. Descending limb ends between 1 and 2. (b) Synthetic melt suite based on the Xol#80 case for Mauna Kea. Small open symbols are less reliable. D_{fit} minimum range is 4.8–5.0.

reasonable selections of C_o^{La} and, thus, solution of the inverse. As expected from the raw data, Mauna Kea (red) and Kiekie (purple) have substantial differences. A synthetic analog of Mauna Kea (blue), made with about 3% error, is reassuringly similar to Mauna Kea. It is plotted before Mauna Kea and partially hidden.

The top row in Figure 8 shows the mantle minerals versus C_o^{La}. Dgt, Dcpx and Dopx increase with C_o^{La} and so olivine must decrease to sum to 100%,. The Dol variation is a rotated mirror image of Dopx. The increases in Dgt and Dcpx versus C_o^{La} are expected given Equation 8 and the higher partition coefficients for gt and cpx compared to opx and ol. The strong linearity for Dgt and Dcpx shows that the boundary conditions are surprisingly effective in filtering the melt mode trials. Each point is the best fit survivor of thousands of melt mode trials. Note that Kiekie is dominated by Dgt and Mauna Kea and its analog is dominated by Dcpx. The mantle modes for olivine and orthopyroxene have considerable noise.

The second row shows the melt modes at each C_o^{La} step. The variations are not linear with C_o^{La}. Pgt increases rapidly at low C_o^{La} and then slowly at higher C_o^{La}. Pcpx decreases at low C_o^{La} and then levels off. Popx and Pol variation have more noise than Dopx and Dol. Dopx and Dol are obtained as D_{fit} is minimized in an optimized least squares procedure. The corresponding Popx and Pol are less controlled. They are part of the melt mode that triggered the mantle mode that survived all the boundary conditions and had the lowest D_{fit}.

The third row is a graphical display of the maximum melt test. The melt% of the basal sample for each suite is proportional to C_o^{La} (Equation 10). The y-axis has mantle mode/melt mode ratios for gt, cpx and opx. These lever rule proportions can be converted to melt % to make the axes identical. A 45° line separates passing trials above the line from failing trials below the line. The minerals making the 45° lines are controlling the maximum melt test. Note that the fail side of a 45° line is sharper than the pass side. Garnet and orthopyroxene control Mauna Kea and clinopyroxene and orthopyroxene control Kiekie. Orthopyroxene was the dominant control (Figure 7b) for Mauna Kea. This is surprising but opx is paired with gt for Mauna Kea and cpx for Kiekie. It is likely that the larger dispersion in Dopx and Popx causes the preponderance of trials to fail for opx. The maximum melt test creates the 45° lines. Equation 8 raises the $\boldsymbol{D}_o^i$ vector as C_o^{La} increases, causing Dgt, Dcpx and Dopx to increase. The software sorts through the melt mode grid and finds the $\boldsymbol{P}^i$ vector that places the D/P of the controlling mineral onto a 45° line. The linearity of the Dopx/Popx plot is especially striking given the scatter in the Popx and Dopx plots above it.

The panels of the fourth row indicate that there are characteristic Dgt/Dcpx and Dcpx/Dopx ratios for Kiekie and Mauna Kea. The Dcpx/Dopx ratio does not vary with C_o^{La} and is substantially higher for Mauna Kea. The Dgt/Dcpx ratio is much higher for Kiekie than for Mauna Kea. The Pgt/Pcpx ratios mimic the shapes of the Dgt/Dcpx ratios. Mauna Kea's Pgt/Pcpx ratio emerges near $C_o^{La} = 1.0$ as the Dgt value becomes positive. For Kiekie (purple), all the ratio plots in the fourth row have extended flat sections above $C_o^{La} = 2.5$ Kiekie also has flat sections in Pgt and Pcpx versus C_o^{La}.

7. C_o^{La} Selections

7.1. Mauna Kea

The normal unperturbed Mauna Kea traverse (Xol#100 in Figures 9a–9c) ends at $C_o^{La} = 4.5$, which is the best choice for C_o^{La}. We also made three perturbed traverses by setting maximum values for *Dol#*. The distortion reduced Dol and Dopx noise, allowing many more trials to be viable. Distortion increased D_{fit} values at the start of the Mauna Kea traverses (Figure 9a). The perturbed traverses eventually merge with or cross the normal traverse between $C_o^{La} = 4$ to 5. For all traverses D_{fit} initially descends smoothly as C_o^{La} increases. In two perturbed traverses D_{fit} ascends after passing an apparent D_{fit} minimum. Our ideal traverse would be symmetric with a descending limb and an ascending limb separated by a D_{fit} minimum identifying C_o^{La}.

Pol varies systematically with C_o^{La} in the perturbed traverses (Figure 9b). All three traverses start with Pol <2, clearly clustered in a lower edge effect. The upper edge effect is not as clear but is interpreted as (Pol > 18.5). In between, there is a narrow transition where Pol increases with C_o^{La}. In contrast, the normal traverse (not shown) has a random Pol distribution between 0 and 20 and no correlation with C_o^{La}. The steps that have Pol values <2 or >18.5 are small black circles in Figure 9d and ignored in Figure 9c, thereby simplifying the C_o^{La} traverses for Mauna Kea. Figure 9c expands the y-scale by a factor of five over Figure 9a, detailing the differences between the traverses. A few of the steps in the normal traverse are lost to the Pol edge effect, but none in the critical region where the traverse ends. Most of the perturbed steps are lost. The ones that remain are in or near the path of the normal traverse (Figure 9d). There is now a composite Mauna Kea traverse (Figure 9c) with both a descending limb, featuring the Xol#100 and Xol#90 traverses, and an ascending limb, featuring the Xol#80 traverse. The Xol#85 traverse links the two limbs.

The Xol#90 traverse (blue) is below the normal traverse until about $C_o^{La} = 4.0$, where it jumps up and over to the normal traverse (Figure 9c). This behavior is explained in Figures 9d and 9b. The horizontal lines in Figure 9d are steps with fixed Dol#. Setting a maximum Dol# caused all steps to have that value if the normal traverse has a higher Dol# at the same C_o^{La}. The array made by the normal traverse descends across the Xol#90 traverse. The systematic increase in Pol (blue in Figure 9b) occurs as the normal array intersects Xol#90. Just as the blue Pol steps reach the upper limit in 9b, the Dol# limit is no longer in effect and the remaining five Xol#90 steps are unperturbed with random variation. The Xol#90 traverse merges with the normal traverse and provides an identical result (Table 4). The other two perturbed traverses are not crossed by the normal array and do not have any unperturbed steps. Therefore, we consider the attractive minima they make less reliable but we include the results for these two traverses in Table 4. The perturbed traverses forced Pol to extreme values and highlighted the usefulness of carefully monitoring traverse results to eliminate distortions caused by reaching range limits.

The actual Dol# for Mauna Kea is clearly lower than 90 and close to 85. The golden section optimization used a tolerance of 0.5% that reduced the effective restriction by roughly 1%, so the actual value for Xol#85 is 84.1. The Dol# result for the Xol#100 traverse is just higher at 85.8, which is a decent estimate for Mauna Kea's Dol# (Table 4). The Xol#85 traverse is just below that and does not merge with the normal traverse.

The normal traverse and the Xol#90 traverse end at C_o^{La} of 4.5, which is the best estimate for the minimum D_{fit}. At higher values of C_o^{La}, all Xol#100 and Xol#90 trials fail. The Xol#85 traverse extends across the path of the normal traverse in Figure 9d, but all the steps are locked in at a Dol# of 84.1. The Xol#85 traverse ends at 5.95 and all trials fail at higher C_o^{La} values. Xol#80 traverse is below the normal traverse. Its Dol# is about 79, which is well below the likely Dol# value for Mauna Kea.

Fifteen melt mode steps, unaffected by Dol# restriction, make an inclined array in Figure 9e at about 18% Pcpx. These steps have the lowest D_{fit} values for the two traverses with unperturbed steps. The array is caused by a consistent 18% proportion of Pcpx and random variation in Pol. The distribution of fractionation corrected lava (Figure 9f) in a projection suitable for tholeiitic magmas (Herzberg & O'Hara, 1998) is nearly the same as the distribution of lowest D_{fit} steps in Figure 9e. The field of potential melt modes deduced from REE data coincides with the field of melts in equilibrium with olivine at Fo 90.3.

By a wide margin, the Mauna Kea model is superior to the other suites for which we were able to obtain valid traverses. The normal traverse and the perturbations from Xol# restrictions locate a D_{fit} minimum, C_o^{La}, and, surprisingly, the Dol#. All other melt model parameters follow. The melt mode proportions, are consistent with the lava compositions, corrected for fractionation (Figures 9e and 9f).

7.2. Kiekie

Kiekie has no well-defined D_{fit} minima in the C_o^{La} traverses examined, (Xol#100, 95 and 90). Restricting the maximum *Dol#* did not expand the range of valid C_o^{La} values as was the case for Mauna Kea. Instead, the *Dol#* variation for the restricted cases is constant until reaching the field defined by the normal case. Upon reaching the normal field, the restricted cases simply merge with it. Therefore, the only useful case is the normal case, Xol#100.

The Kiekie traverse (Figure 10a) begins with the expected initial decline in D_{fit}. The traverse then flattens to a near constant level with considerable noise. Figure 10a includes a regression line through the flat section, the C_o^{La} range from 2.5 to 5. The descending limb reached the line at about 1.0. By 2.0, the center of the descending limb reaches the regression line. We pick three C_o^{La} steps that cover the minimum area, 1.0, 1.5 and 2.0 (Table 4). Figure 10a provides a one-sided minimum, a lower limit. At Mauna Kea, the preferred Xol#100 and Xol#90 cases are also one-sided, but the range of valid C_o^{La} terminates, which is a stronger control than the continuation at a near constant level at Kiekie.

The uncertainty in the Kiekie minimum is disapointing. Perhaps there is an unrecognized boundary condition that would terminate the traverse or cause D_{fit} to increase with C_o^{La}. It is also possible that the inverse is less sensitive in a mantle that has so much olivine and garnet and so little clinopyroxene (Table 4). The HREE data appear excellent, but Lu was excluded from the inverse model because I^{Lu} is close to zero (Figure 1c) and the intercept vector is in the divisor for Equations 7 and 8. Running the model with Lu included, results in a pyroxenite mantle with C_o^{La} above 4. Primelt3 found many Kiekie samples consistent with a peridotite mantle. Therefore, we prefer the model in Table 4, which was run without Lu.

The pattern of failure for Kiekie is simpler than that of Mauna Kea. The traverse starts at $C_o^{La} = 0.2$, well below the chondrite level. Most of the 61,628 trials failed because of negative garnet in the mantle mode. These failures rapidly decrease and then end at 1.35. Negative clinopyroxene occurs between 0.35 and 1.35 with a peak at 0.65. Maximum melt failures are present at the start and steadily increase through the traverse, but never get quite high enough to terminate the traverse.

7.3. Synthetic Models for Mauna Kea

Mauna Kea's normal traverse has its first valid C_o^{La} step at 1.0 and last at 4.5. Over this range, D_{fit} decreases from 11.8×10^{-6} to 9.2×10^{-6}, a 28% change. The Kiekie traverse has a weaker signal from 8.53×10^{-5} to 8.1×10^{-5}. These weak signals would be more convincing if the full range of behaviors can be replicated. Therefore, we modeled Mauna Kea with synthetic suites using random numbers applied in three places. The first determines a melt% based on the mean and standard deviation of the melt model. Second, each synthetic melt gets a sample error S applied uniformly to each element in a sample. Finally, we apply a random element error, E, to each element as it is calculated. These three random numbers generate melt suites that approximate but do not match the Mauna Kea data. Compared with Mauna Kea, the synthetics have less error in the process identification regressions but more irregular patterns in the slope and intercept vectors. A very good synthetic analog of Mauna Kea is shown in Figures 8 and 10b.

The basal D_{fit} error level for Mauna Kea is about 9.2 10^{-6} (Figure 9a), much higher than the basal error level for SYN-S1-E1.22 in Figure 10b, which is about 2.5 10^{-6}. We find that separate randomly generated melt suites, using the same values for melt error, sample error and element error vary by a factor of 5 at the basal error level. Furthermore, 30% of synthetic melt suites fail completely. The synthetic intercept profiles are more jagged than the Mauna Kea profile in Figure 1b and the cause has eluded us. Nevertheless, the synthetic model in Figure 10b behaves like Mauna Kea and has similar results. SYN-S1-E1.22 has a well-developed descending limb that

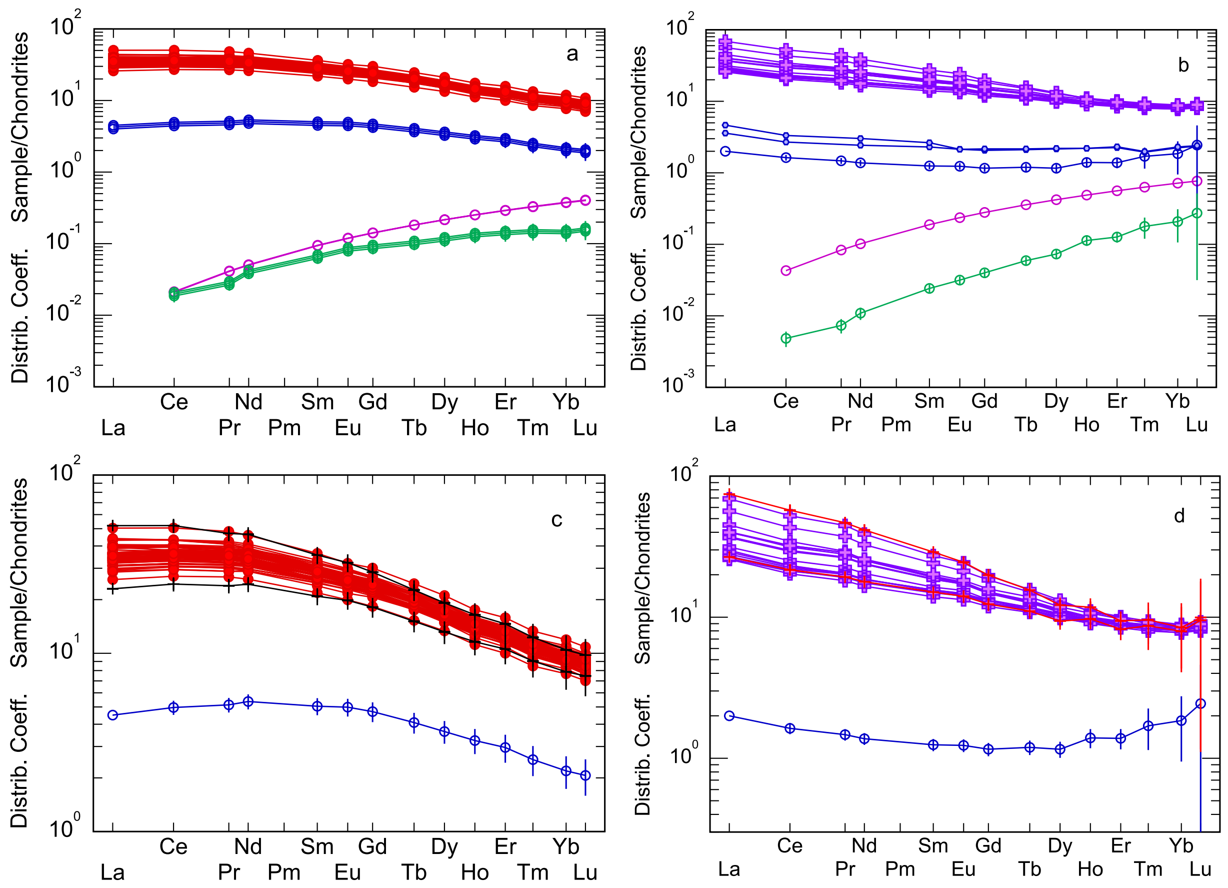

Figure 11. C_o^i D_o^i P^i melt models. Calculated from data in Table 4 and Table S2 in Supporting Information S3. Error bars represent ±1.0 SE. In panels (a) and (b) the profile order is lava field at the top, followed by C_o^i, P^i, D_o^i. (a) Mauna Kea with three models for C_o^{La} values 4.5, 4.25, and 4.0. C_o^i in blue. $\boldsymbol{D_o^i}$ in green and $\boldsymbol{P^i}$ in magenta. (b) Submarine Kiekie with one model for C_o^{La} of 2.0. Small blue hexagons are source estimates from Dixon et al. (2008): Model 1 + 0.2% Car and Model 1 + 0.1% Car. Other symbols as in a. (c) Melt brackets (black crosses) for Mauna Kea from $C_o^{La} = 4.5$ model and melts of 8% and 19%. (d) Melt brackets (red crosses) for Kiekie from $C_o^{La} = 2.0$ model and melts of 2.7% and 7.7%.

reaches a minimum at about C_o^{La} step 4.8. The traverse ends at step 5.2. It has a higher proportion of steps affected by the Pol edge effect than the normal traverse for Mauna Kea. It is superior to Mauna Kea in having a short ascending limb, creating a D_{fit} minimum. The SYN model does not match the Xol#80 input. However, we expect synthetics with errors to deviate from the input and consider the amount of deviation in Table 4 acceptable.

8. Modeling Results for Hawaii Shield and Post-Shield Lavas

8.1. Mauna Kea

The normal traverse locates C_o^{La} at 4.5. This point is the minimum D_{fit} and the last valid point of the traverse. This solution is labeled Mauna Kea preferred in Table 4. The Xol#90 traverse merges with the preferred case and is equivalent. The other Mauna Kea traverses in Figure 9 give similar estimates of C_o^{La} (Table 4) but are less reliable. The variations in Table 4 reflect the relationship between C_o^{La}, extent of melting and mantle mineralogy expected from Equations 8, 10 and 11 and Figure 8.

Mauna Kea's bulk distribution coefficients for mantle and melt appear close in Figure 11a but Table 4 shows that this is not a case of modal melting. The Mauna Kea source (Figure 11a) is asymmetric and bowed upward. The peak occurs at Nd, the LREE limb descends to La, and the HREE end at Lu is substantially lower than the LREE end. The inverse model in Frey et al. (1991) has the same shape but has relative values with the HREE set to around 1. Our HREE values are 2–3 times higher, so we need a higher degree of melting, about 19%, to reproduce the base of the data array (Figure 11c). The top of the data array is made with 8% melting. Our melt percentages seem reasonable, and our results do not require an assumption about the mantle composition.

Frey et al. (1991) reported a puzzling increase in residual clinopyroxene as the % melt increased. We find the same positive correlation in our traverses, but our approach is different. In our case, the positive correlation is expected and easily explained. C_o^{La} increases along a traverse. Higher C_o^{La} lifts both the source profile and the $\boldsymbol{D}_o^i$ profile. Higher $\boldsymbol{D}_o^i$ requires more cpx and higher C_o^i moves the source closer to the data and so the % of melt also must increase. Overall, our results are compatible with those of Frey et al. but give values for initial source concentration and degree of melting that derive from observed REE patterns.

8.2. Kiekie

The Kiekie C_o^i D_o^i P^i models in Table 4 have more than twice as much garnet in both the mantle and melt modes than Mauna Kea. The amount of olivine in the mantle mode is very high.

The C_o^i profile for $C_o^{La} = 2.0$, shown in Figures 11b and 11d, starts at La = 2. The $C_o^{La} = 1.0$ model for Kiekie (Figure 4c) is lower, but parallel to the model in Figure 11b. The C_o^i profiles for Kiekie bend up, whereas Mauna Kea profiles bend down. The bulk distribution coefficient profiles also differ in shape and location. Mauna Kea has a higher and less steep $\boldsymbol{D}_o^i$ profile whereas Kiekie has a higher $\boldsymbol{P}^i$ profile. The Kiekie melt modes in Table 4 have very large proportions of orthopyroxene. We do not compare Kiekie's melt modes and primary magmas because the anorthite projection used for Mauna Kea is not appropriate for alkaline magmas.

The C_o^i profile for submarine Kiekie in Figure 11b has the same shape as sources proposed in Table 7c of Dixon et al. (2008). Their estimates are the small blue hexagons in Figure 11b. From La to Er our profiles are about a factor of two lower, so our result requires smaller degrees of melting. The HREE of our source in Figure 11b has large errors, related to low intercepts in the process identification regressions. These errors make the steep slope in our HREE profile less reliable. The C_o^{La} 2.0 model in Table 4 brackets the Kiekie data (Figure 11d) with melts of 2.7% and 7.7%, which are lower than the 4%–13% found by Dixon et al. (2008). The refractory mantle, assumed for forward models by Dixon et al. (2008), has more clinopyroxene than our inverse result (Table 4). Overall, we consider our model to be in reasonable agreement with Dixon et al. (2008).

9. Discussion

9.1. Bracketing the Magma Suites

Inverse models must be able to bracket the input data arrays, but success does not imply a unique solution. The Mauna Kea and Kiekie models in Table 4 and Supplemental Table 2 reproduce the fractionation corrected arrays of actual data for the two suites (Figures 11c and 11d). It is probable that many adjacent C_o^{La} steps in Figure 9c will by visual comparison at least, reproduce the data arrays for Mauna Kea in a standard log based REE plot. However, before adding a maximum melt test, the software routinely picked trials with the lowest D_{fit} that failed to match the data arrays. Figure 7d shows several hundred trials that fail the max melt test but have lower D_{fit} than the passing trials. The maximum melt test both narrowed the field of solutions and made it simple to bracket the input data.

9.2. D_{fit}, Boundary Conditions, Reliability, and Applicability of Results

Throughout the inverse model, D_{fit} compares possible solutions created from the melt mode grid. The observed $\boldsymbol{D}_o^i$ minus calculated $\boldsymbol{D}_c^i$ comparison is a new insight and a useful contribution. However, we proved that D_{fit} is inadequate by itself (e.g., Figures 6d and 7d). By using a graphical approach based on searches, we discovered boundary conditions that remove most trial melt modes and reveal inverse paths with consistent patterns. The most important is an initial decrease in the value of D_{fit} as C_o^{La} increases. The end of this descent is the preferred pick for C_o^{La}. The inverse solution combines D_{fit}, boundary conditions and characteristic behavior of inverse paths.

Changing assumptions and locating critical samples will modify the results. For example, we tested the sensitivity of mantle modes to changes in the partition coefficients of garnet and clinopyroxene in the range of ±10%. The changes in mantle modes at minimum D_{fit} were nearly linear with increases in partition coefficients causing decreases in mantle mode. If the slope adjustment (Section 2.3) is turned off, the C_o^{La} determined for Mauna Kea increases from 4.5 to 4.85. Similarly, turning off the $\boldsymbol{D}_o^{Ce} < \boldsymbol{P}^{Ce}$ boundary condition increases Mauna Kea's C_o^{La} from 4.5 to 4.9. Because the maximum melt test is tied to the basal sample, C_o^{La} can be lowered by finding a new sample with a lower REE profile (requiring a higher % melt). At $C_o^{La} = 4.5$, the basal sample SRO622–7.10 has an estimated 18.7% melt. To lower C_o^{La} by 0.33 a new sample will need a melt of 19.7%.

Based on our experience, we rank the results of the inverse as follows. The most reliable result is the shape of the source profile, C_o^i, calculated at $C_o^{La} = 1$. The source shape is based only on the choice of melt mode and the intercept vector, $\boldsymbol{I}^i$. Second is the shape of the $\boldsymbol{D}_o^i$ profile which has the added uncertainty of the slope vector, $\boldsymbol{S}^i$. The C_o^{La} determination is third. The quantitative source (blue in Figure 11) is fourth. The quantitative bulk distribution coefficient for the mantle (green in Figure 11) is fifth and the mantle modes are at the same level. The bulk distribution coefficient of the melt, $\boldsymbol{P}^i$, and the melt modes are less reliable because they are an input that is not calculated but rather remains as a survivor. Within the melt and mantle modes, garnet and clinopyroxene and the sum of olivine and orthopyroxene are well determined, but *Dol#* and *Pol#* are less reliable.

Because the low partition coefficients for olivine and orthopyroxene cause uncertainty in the determination of their relative proportions in mantle and melt modes, we can't resolve one of the major questions we sought to answer concerning Hawaiian main stage magmas. Strong arguments from trace element and isotopic data favor peridotite melting with only a few percent of more silicic subducted components (e.g., Hofmann et al., 1984; Putirka et al., 2011; White & Hofmann, 1982; Willbold & Stracke, 2006). Several petrological studies have concluded that peridotite melting cannot produce the silica-rich tholeiites common to Hawaiian volcanoes. Hauri (1996) argued for a mix of peridotite and pyroxenite melts. Sobolev et al. (2005) argued that high Ni concentrations in olivine from many hot spot lavas are inconsistent with peridotite melting. Herzberg (2006) used petrological modeling to argue that both the high and low silica magmas at Mauna Kea are pyroxenite melts. The REE inverse model for Mauna Kea does not resolve the peridotite/pyroxenite source issue. The code was designed for a garnet lherzolite mantle and the Mauna Kea results in Figures 9 and 10 and Table 4 indicate a peridotite source. The code allows a restriction on the maximum proportion of olivine, an upper limit on *Dol#*, but the unrestricted, higher olivine case is superior (Figure 9).

The Mauna Kea source, inferred by the inverse model, is a lherzolite with a small amount of garnet. Therefore, we favor the two-stage model of Wagner and Grove (1998). The first stage produces a low silica basalt by melting of garnet lherzolite. This sets the REE profiles. The second stage is a melt/harzburgite reaction as the primary melt rises into the lithosphere, crystallizing olivine and adding silica to the melt. The reaction adds about 15% to the melt volume, diluting all the REEs. However, the low partition coefficients of the REE for olivine and orthopyroxene cause only minor changes in REE ratios, preserving the characteristics of the initial melt. Correcting for a 15% dilution would increase the mantle modes of garnet and clinopyroxene by similar percentages.

9.3. Magma Suites That Preserve Evidence of Melt Processes

Batch melts separated from a similar source at different extents of melting will produce an array of REE profiles with a funnel shape with a wide end in the LREE. The Kiekie REE profiles fit this expectation. These high-quality data allowed a one-sided D_{fit} minimum. The Mauna Kea REE profiles indicate a lower range of melt extents but allowed a better model. The large number of samples improved this model. Both suites came from a hot spot. The Mauna Kea lava were buried after relatively short intervals exposed at the surface, reducing the chance for REE alteration in a tropical climate. Submarine glasses from Kiekie may have also been protected from alteration.

The Mauna Kea HSDP2 drill core (Figure 2) sampled several magma suites with different behaviors. Near the top of the section are the geochemically distinct Mauna Loa samples. The rest of the section comprises three Mauna Kea suites that have clear separation in MgO versus SiO_2 (Figure 2a). The top of the Mauna Kea section includes six samples with lower SiO_2 and higher La/Lu (Figure 2d). These more alkaline samples are distinct. Interbedded with them are four low silica samples with MgO <10% and $La_N/Lu_N < 5$. These uppermost samples erupted as Mauna Kea was moving off the hot spot. The rest of the Mauna Kea section has an interesting contrast in the MgO variation between high-silica and low-silica samples. The high-silica samples maintain a wide range of MgO throughout the section, about 7%–27% MgO. The low silica samples start out with an MgO range of 10%–17%. Near the top, the range has shifted higher to between 17% and 27% MgO. Much of the MgO variation is the result of sorting of olivine crystals and both suites are on olivine control lines. The expansion of the olivine primary phase volume with decreasing pressure may be a factor as well. The narrower range and gradual evolution of the low silica samples is consistent with an evolved magma chamber and a shorter ascent for erupting magma. The high silica suite does not change with time. The large MgO range suggests a long path allowing greater crystallization and sorting of olivine crystals during ascent. The low silica suite does not allow an inverse because removing the effects of olivine removal/accumulation removes nearly all the REE variation (Feigenson et al., 2003). The high silica samples seem to be separate magmas produced by different extents of melting that rise from mantle depth. They avoid the homogenization that occurs in magma chambers and allow melting systematics to reach the surface. The short Mauna Loa section looks like the high silica section at Mauna Kea and is a good candidate for additional sampling to test melting models.

Research on the melt dynamics of the HSDP2 suites may provide information on the conditions that sometimes allow melting processes to be recognized. Homogenization by magma mixing needs to be minimized, so the plumbing system needs rapid ascent and minimal mixing. It is also curious that Mauna Kea's high silica suite has a normal distribution of melt percentages, but the Kiekie suite appears skewed to high percentages.

The new inverse procedure described in this paper builds on previous work on Hawaiian lava suites by injecting a quantitative approach to determining mantle composition and melting parameters. Our earlier attempts at inverse modeling are reproduced but in much finer detail, allowing actual values for source mineralogy and degree of melting. The technique relies on the assumption of batch partial melting, which is likely an oversimplification of how melt generation occurs. We note that other geophysical melting models, such as accumulated fractional melting, give broadly similar results to those here, while fractional melting models with no accumulation do not reproduce the observed lava REE compositions (Feigenson et al., 1996, 2003).

10. Conclusions

Careful attention to minimize the effects of post melting processes like accumulation, fractional crystallization, mixing and weathering is a prerequisite for inverse modeling.

The assumption of perfect incompatibility of La decreases the LREEs in the $\boldsymbol{D}_o^i$ profile but the shift can be calculated and the profile corrected.

Boundary conditions greatly reduce the volume within a melt mode grid that makes valid mantle modes. Before calculating a mantle mode, two tests provide effective limits. The first is to limit the number of olivine entering melts to 20%. The second uses limiting ratios of HREE to eliminate profiles inconsistent with the partition coefficients (Figure 7a).

C_o^{La} restricted earlier applications of this inverse approach to relative results. Quantitative results require an additional constraining equation. Equation 13 is useful for ranking melt mode trials. If $\boldsymbol{D}_o^i$ can be inverted to estimate mantle mineralogy, then D_c^i is readily calculated from mantle mode times partition coefficients. D_{fit}, the difference between observed $\boldsymbol{D}_o^i$ and calculated $\boldsymbol{D}_c^i$, will be a minimum when the estimated mantle mineralogy is closest to the actual mineralogy of the source. This works only as part of a constrained model, where invalid mantle and melt modes are eliminated by boundary conditions.

Olivine and orthopyroxene typically make up most of the mantle, but their similarly low partition coefficients prevent separately determining them via least squares methods. Combining ol + opx allows calculation of a mantle mode for gt, cpx and ol + opx. Golden section optimization then selects the ol and opx proportions that minimize D_{fit}. Despite these efforts, many melt mode trials generate negative garnet or clinopyroxene in the mantle mode and fail.

The maximum melt test (e.g., magenta in Figures 6d and 7d) eliminates trials whose D_{fit} values are lower than the eventually selected minimum D_{fit}. This test assumes that melting ends when a phase is used up. A sophisticated approach to melting would be an improvement, but this simplifying assumption works. The final two boundary conditions compare the $\boldsymbol{D}_o^i$ profile to the $\boldsymbol{P}^i$ profile and fail the trial if $\boldsymbol{D}^i > \boldsymbol{P}^i$. This condition may be too restrictive for garnet-rich sources.

Traverse diagrams (Figures 8–10) locate D_{fit} minima and thus determine C_o^{La}. There are obvious artifacts caused by the step-wise nature of the searches through C_o^{La} and the melt mode grid. More sophisticated mathematics can alleviate this noise, but the awkward and time-consuming searches allowed us to visualize the interactions between S^i, I^i, $\boldsymbol{P}^i$ and boundary conditions that create inverse paths through melt and mantle mode space.

Our Hawaiian results are broadly compatible with previous work. Our sources have the same shapes as previous source profiles for Mauna Kea and Kiekie. Our Kiekie source is about a factor of two lower than the forward model of Dixon et al. (2008) and our estimated degree of melting is lower by a similar factor. The HREE in our Mauna Kea source is about a factor of 2–3 higher than the model of Frey et al. (1991). Our estimated degree of melting is correspondingly higher.

Data Availability Statement

The REE inverse program is available in two modes. The inverse subroutine Codopi is listed in Supporting Information S2 and at https://zenodo.org/records/11182237 (Carr et al., 2024). The inverse is part of Igpet (Carr & Gazel, 2017), which has been freely available on the Igpet site since 2016 (Carr, 2024). MJC plans to maintain the site for several more years. The site has Windows and OSX versions available for free download. The inverse is in the model option when a REE plot is made. Example data and an explanatory note are part of the Igpet download.

Acknowledgments
We thank Bill White for helpful suggestions on an earlier draft of the manuscript. S. Carr made useful suggestions on optimization methods. The suggestions of two reviewers clarified the manuscript. This work was supported in part by NSF Award No. EAR 1826673 to EG.

References

Albarède, F. (1983). Inversion of batch melting equations and the trace element pattern of the mantle. *Journal of Geophysical Research*, *88*(B12), 10573–10583. https://doi.org/10.1029/jb088ib12p10573

Albarède, F. (1995). *Introduction to geochemical modeling*. Cambridge University Press. https://doi.org/10.1017/CBO9780511622960

Albarède, F., & Tamagnan, V. (1988). Modelling the recent geochemical evolution of the Piton de la Fournaise volcano, Réunion Island. *Journal of Petrology*, *29*(5), 997–1030. https://doi.org/10.1093/petrology/29.5.997

Beattie, P. (1994). Systematics and energetics of trace-element partitioning between olivine and silicate melts: Implications for the nature of mineral/melt partitioning. *Chemical Geology*, *117*(1–4), 57–71. https://doi.org/10.1016/0009-2541(94)90121-X

Blundy, J., & Wood, B. (2003). Partitioning of trace elements between crystals and melts. *Earth and Planetary Science Letters*, *210*(3–4), 383–397. https://doi.org/10.1016/S0012-821X(03)00129-8

Brown, E. L., Petersen, K. D., & Lesher, C. E. (2020). Markov chain Monte Carlo inversion of mantle temperature and source composition, with application to Reykjanes peninsula, Iceland. *Earth and Planetary Science Letters*, *532*, 116007. https://doi.org/10.1016/j.epsl.2019.116007

Bryce, J. G., Depaolo, D. J., & Lassiter, J. C. (2005). Geochemical structure of the Hawaiian plume: Sr, Nd, and Os isotopes in the 2.8 km HSDP-2 section of Mauna Kea volcano. *Geochemistry, Geophysics, Geosystems*, *6*(9), Q09G18. https://doi.org/10.1029/2004GC000809

Carr, M. J. (2024). Igpet software for graphics and modeling in igneous petrology [Software]. *Google Sites*. https://sites.google.com/site/tsigpetteaching/

Carr, M. J., Feigenson, M. D., & Gazel, E. (2024). Codopi inverse model subroutine (Zenfix version) [Software]. *Zenodo*. https://zenodo.org/records/11182237

Carr, M. J., & Gazel, E. (2017). Igpet software for modeling igneous processes: Examples of application using the open educational version. *Mineralogy and Petrology*, *111*(2), 283–289. https://doi.org/10.1007/s00710-016-0473-z

Clague, D. A., & Frey, F. A. (1982). Petrology and trace element geochemistry of the Honolulu Volcanics, Oahu: Implications for the oceanic mantle below Hawaii. *Journal of Petrology*, *23*(3), 447–504. https://doi.org/10.1093/petrology/23.3.447

DePaolo, D. J., & Stolper, E. M. (1996). Models of Hawaiian volcano growth and plume structure: Implications of results from the Hawaii Scientific Drilling Project. *Journal of Geophysical Research*, *101*(B5), 11643–11654. https://doi.org/10.1029/96jb00070

DePaolo, D. J., Thomas, D. M., Stolper, E. M., & Garcia, M. O. (1999). *Hawaii, scientific drilling project: Core logs and summarizing data, rep*. Calif. Inst. Of Technol.

Dixon, J., Clague, D. A., Cousens, B., Monsalve, M. L., & Uhl, J. (2008). Carbonatite and silicate melt metasomatism of the mantle surrounding the Hawaiian plume: Evidence from volatiles, trace elements, and radiogenic isotopes in rejuvenated-stage lavas from Niihau, Hawaii. *Geochemistry, Geophysics, Geosystems*, *9*, Q09005. https://doi.org/10.1029/2008GC002076

Feigenson, M. D., Bolge, L. L., Carr, M. J., & Herzberg, C. T. (2003). REE inverse modeling of HSDP2 basalts: Evidence for multiple sources in the Hawaiian plume. *Geochemistry, Geophysics, Geosystems*, *4*(2), 8706. https://doi.org/10.1029/2001GC000271

Feigenson, M. D., Hofmann, A. W., & Spera, F. J. (1983). Case studies on the origin of basalt. 2. The transition from tholeiitic to alkalic volcanism on Kohala volcano, Hawaii. *Contributions to Mineralogy and Petrology*, *84*(4), 390–405. https://doi.org/10.1007/bf01160290

Feigenson, M. D., Patino, L. C., & Carr, M. J. (1996). Constraints on partial melting imposed by rare earth element variations in Mauna Kea basalts. *Journal of Geophysical Research*, *101*(B5), 11815–11829. https://doi.org/10.1029/95jb03847

Fodor, R. V., Frey, F. A., Bauer, G. R., & Clague, D. A. (1992). Ages, rare-earth element enrichment, and petrogenesis of tholeiitic and alkalic basalts from Kahoolawe Island, Hawaii. *Contributions to Mineralogy and Petrology*, *110*(4), 442–462. https://doi.org/10.1007/bf00344080

Frey, F. A., Garcia, M. O., Wise, W. S., Kennedy, A., Gurriet, P., & Albarede, F. (1991). The evolution of Mauna Kea volcano, Hawaii: Petrogenesis of tholeiitic and alkalic basalts. *Journal of Geophysical Research*, *96*(B9), 14347–14375. https://doi.org/10.1029/91jb00940

Garcia, M. O., Swinnard, L., Weis, D., Greene, A. R., Tagami, T., Sano, H., & Gandy, C. E. (2010). Petrology, geochemistry and geochronology of Kaua'i lavas over 4·5 Myr: Implications for the origin of rejuvenated volcanism and the evolution of the Hawaiian plume. *Journal of Petrology*, *51*(7), 1507–1540. https://doi.org/10.1093/petrology/egq027

Hauri, E., Wagner, T. P., & Grove, T. L. (1994). Experimental and natural partitioning of Th, U, Pb and other trace elements between garnet, clinopyroxene and basaltic melts. *Chemical Geology*, *117*(1–4), 149–166. https://doi.org/10.1016/0009-2541(94)90126-0

Hauri, E. H. (1996). Major element variability in the Hawaiian mantle plume. *Nature*, *382*(6590), 415–419. https://doi.org/10.1038/382415a0

Herzberg, C., & Asimow, P. D. (2015). PRIMELT3 MEGA.XLSM software for primary magma calculation: Peridotite primary magma MgO contents from the liquidus to the solidus. *Geochemistry, Geophysics, Geosystems*, *16*(2), 563–578. https://doi.org/10.1002/2014GC005631

Herzberg, C., & O'Hara, M. J. (1998). Phase equilibrium constraints on the origin of basalts, picrites, and komatiites. *Earth and Planetary Science Letters*, *44*(1–2), 39–79. https://doi.org/10.1016/S0012-8252(98)00021-X

Herzberg, C. T. (2006). Petrology and thermal structure of the Hawaiian plume from Mauna Kea volcano. *Nature*, *444*(7119), 605–609. https://doi.org/10.1038/nature05254

Hofmann, A. W., & Feigenson, M. D. (1983). Case studies on the origin of basalt. I. Theory and reassessment of Grenada basalts. *Contributions to Mineralogy and Petrology*, *84*(4), 382–389. https://doi.org/10.1007/bf01160289

Hofmann, A. W., Feigenson, M. D., & Raczek, I. (1984). Case studies in the origin of basalt. III. Petrogenesis of the Mauna Ulu eruption, Kilauea, 1969±1971. *Contributions to Mineralogy and Petrology*, *88*(1–2), 24–35. https://doi.org/10.1007/bf00371409

Huang, S., & Frey, F. A. (2003). Trace element abundances of Mauna Kea basalt from Phase 2 of the Hawaiian Scientific Drilling Project: Petrogenetic implications of correlations with major element content and isotopic ratios. *Geochemistry, Geophysics, Geosystems*, *4*(6), 8711. https://doi.org/10.1029/2002GC000322

Kelemen, P. B., Dick, H. J. B., & Quick, J. E. (1992). Formation of harzburgite by pervasive melt/rock reaction in the upper mantle. *Nature*, *358*(6388), 635–641. https://doi.org/10.1038/358635a0

Langmuir, C. H., Vocke, R. D., Hanson, G. N., & Hart, S. R. (1977). A general mixing equation: Applied to the petrogenesis of basalts from Iceland and the Reykjanes Ridge. *Earth and Planetary Science Letters*, *37*(3), 380–392. https://doi.org/10.1016/0012-821x(78)90053-5

Liu, B., & Liang, Y. (2017). An introduction of Markov chain Monte Carlo method to geochemical inverse problems: Reading melting parameters from REE abundances in abyssal peridotites. *Geochimica et Cosmochimica Acta*, *203*, 216–234. https://doi.org/10.1016/j.gca.2016.12.040

McDonough, W., & Sun, S. S. (1995). The composition of the Earth. *Chemical Geology*, *120*(3–4), 223–253. https://doi.org/10.1016/0009-2541(94)00140-4

McKenzie, D., & O'Nions, R. K. (1991). Partial melt distributions from inversion of rare earth element concentrations. *Journal of Petrology*, *32*(5), 1021–1091. https://doi.org/10.1093/petrology/32.5.1021

Minster, J. F., & Allègre, C. J. (1978). Systematic use of trace-elements in igneous processes. III. Inverse problem of batch partial melting in volcanic suites. *Contributions to Mineralogy and Petrology*, *68*(1), 37–52. https://doi.org/10.1007/bf00375445

Oliveira, B., Afonso, J. C., & Klöcking, M. (2021). Melting conditions and mantle source composition from probabilistic joint inversion of major and rare earth element concentrations. *Geochimica et Cosmochimica Acta*, *315*, 251–275. https://doi.org/10.1016/j.gca.2021.09.008

Onuma, N., Higuchi, H., Wakita, H., & Nagasawa, H. (1968). Trace element partition between two pyroxenes and the host lava. *Earth and Planetary Science Letters*, *5*, 47–51. https://doi.org/10.1016/s0012-821x(68)80010-x

Putirka, K., Ryerson, F. J., Perfit, M., & Ridley, W. I. (2011). Mineralogy and composition of the oceanic mantle. *Journal of Petrology*, *52*(2), 279–313. https://doi.org/10.1093/petrology/egq080

Rhodes, J. M., & Vollinger, M. J. (2004). Composition of basaltic lavas sampled by phase-2 of the Hawaii Scientific Drilling Project: Geochemical stratigraphy and magma types. *Geochemistry, Geophysics, Geosystems*, *5*(3), Q03G13. https://doi.org/10.1029/2002GC000434

Shaw, D. M. (1970). Trace element fractionation during anatexis. *Geochimica et Cosmochimica Acta*, *34*(2), 237–243. https://doi.org/10.1016/0016-7037(70)90009-8

Sobolev, A. V., Hofmann, A. W., Sobolev, S. V., & Nikogosian, I. K. (2005). An olivine-free mantle source of Hawaiian shield basalts. *Nature*, *434*(7033), 590–597. https://doi.org/10.1038/nature03411

Stolper, E., Sherman, S., Garcia, M., Baker, M., & Seaman, C. (2004). Glass in the submarine section of the HSDP2 drill core, Hilo Hawaii. *Geochemistry, Geophysics, Geosystems*, *5*(7), Q07G15. https://doi.org/10.1029/2003GC000553

Treuil, M., & Joron, J. L. (1975). Utilisation des elements hygromagmatophiles pour la simplification de la modélisation quantitative des processus magmatiques: Exemples de l'Afar et de la Dorsale Médioatlantique. *Societa Italiana Mineralogia e Petrologia*, *31*, 125–174.

Van Westrenen, W., Blundy, J., & Wood, B. (1999). Crystal-chemical controls on trace element partitioning between garnet and anhydrous silicate melt. *American Mineralogist*, *84*(5–6), 838–847. https://doi.org/10.2138/am-1999-5-617

Wagner, T. P., & Grove, T. L. (1998). Melt/harzburgite reaction in the petrogenesis of tholeiitic magma from Kilauea volcano, Hawaii. *Contributions to Mineralogy and Petrology*, *131*, 1–12. https://doi.org/10.1007/s004100050374

White, W. M., & Hofmann, A. W. (1982). Sr and Nd isotope geochemistry of oceanic basalts and mantle evolution. *Nature*, *29*(5860), 821–825. https://doi.org/10.1038/296821a0

Willbold, M., & Stracke, A. (2006). Trace element composition of mantle end-members: Implications for recycling of oceanic and upper and lower continental crust. *Geochemistry, Geophysics, Geosystems*, *7*(4), Q04004. https://doi.org/10.1029/2005GC001005

Zou, H. (1997). Inversion of partial melting through residual peridotites or clinopyroxenes. *Geochimica et Cosmochimica Acta*, *61*(21), 4571–4582. https://doi.org/10.1016/S0016-7037(97)00258-5